Flexural Buckling Curves of High-Strength, Wide-Flange Steel Columns

SHAHRIAR QUAYYUM

ABSTRACT

Rolled shapes using structural steel with a specified yield strength, F_y, of 65 ksi or higher are considered an alternative solution to built-up shapes using conventional steel grades. However, major evidence exists that current design rules (e.g., AISC 360, Eurocode 3) are likely overly conservative for these higher-strength steels with $F_y \geq 65$ ksi—particularly at yield strengths of 80 ksi and above when employed as structural steel columns—due in part to assumptions regarding residual stresses. In order to understand the extent of these conservative predictions and explore if alternative design provisions could be provided to engineers utilizing specific shapes and high-strength materials grade, this study presents comprehensive nonlinear finite element analyses of rolled W-shape columns made from ASTM A992 ($F_y = 50$ ksi) and A913 Grade 80 ($F_y = 80$ ksi) steels. The models incorporate validated multiaxial residual stress distributions, geometric imperfections, and nonlinear material behavior, and are benchmarked against experimental data.

Column flexural buckling curves are developed for a range of cross-sectional geometries and slenderness ratios and compared to predictions from AISC 360 and Eurocode 3 for both major and minor axis buckling. For A992 ($F_y = 50$ ksi), the AISC column curve overestimates the buckling strength for heavier sections and underestimates it for more slender or lightly built shapes, reflecting shape-dependent divergence. For A913 Grade 80 ($F_y = 80$ ksi), simulation results are generally close to AISC predictions, with a 5–14% increase in buckling strength observed, depending on the section geometry and slenderness. The findings generally support the use of AISC 360-22 but suggest refinement might be needed for heavier or high-strength rolled shapes in the inelastic buckling range. The results also highlight the potential need for shape- or grade-specific column curves. Future experimental validation will be essential to confirm these trends and guide potential updates to design standards.

Keywords: high-strength steel, finite element analysis, flexural buckling, initial imperfection, residual stresses, rolled shape, W section.

INTRODUCTION

Rolled shapes using high-strength structural steel (HS3) with a specified yield strength, F_y, of 65 ksi (450 MPa) or higher can provide improvements in cost, speed, simplicity, footprint, performance, and embodied carbon content when applied in lower stories of high-rise buildings and other non-stiffness-controlled structural members such as long span trusses. These hot-rolled shapes are desirable when considering alternative solutions such as built-up shapes using conventional steel grades. Several examples exist in the United States today, where high-strength rolled shapes were selected for columns. A notable example of high-strength, rolled-shape application is the 320 S. Canal project (Union Station Tower) in Chicago, which utilized ASTM A913 (2019b) Grade 80 wide-flange columns in the tower's upper perimeter framing. This marked the first documented use of Grade 80 rolled shapes in a U.S. building project, enabling more compact section sizes and a 20% steel tonnage reduction in upper-story framing. Such applications underscore the growing demand for optimized column design provisions for rolled HS3 products. The readers are also referred to HS3 Ad Hoc Task Group Report on High Strength Steel (AISC, 2019) for other examples. High-strength rolled shape columns have also been used in several major structures worldwide, particularly in high-rise buildings and large infrastructure projects, that showcase how rolled-shape columns (mainly wide-flange beams, H-sections, and hollow structural sections) are incorporated into modern high-strength steel structures to enhance load-bearing capacity, seismic performance, and overall efficiency. Reports have shown that for larger load applications, rolled high-strength steel shapes can save up to 46% of the fabrication cost compared to Gr. 50 built-up members (ArcelorMittal, 2019).

Currently, select producers are capable of rolling plates with a specified yield stress up to 130 ksi using quenching and tempering processes. Hot-rolled wide flange shapes with a specified yield stress up to 80 ksi made by the quenched and self-tempering (QST) process are also available, while other hot-rolled shapes with a specified yield stress of 65 ksi or greater are also available. Although several U.S.-based steel producers are capable of producing these HS3 products, a lack of guidance and standards has seemingly kept designers from implementing HS3 into their

Shahriar Quayyum, Assistant Professor, Department of Civil & Environmental Engineering, Manhattan University, Riverdale, N.Y. Email: shahriar.quayyum@manhattan.edu

Paper No. 2025–06

Table 1. Materials Listed in AISC 360-22, Table A3.1, with $F_y \geq 65$ ksi		
Specified Yield Stress (F_y)	**Standard Designation of Listed Material in AISC 360-22**	**Steel Type and Production Process**
65 ksi (450 MPa)	ASTM A572/A572M Gr. 65 [450], Type 1, 2, or 3	High-strength low-alloy (HSLA) steel
	A709/A709M QST 65 [QST 450]	HSLA steel produced by quenching and self-tempering process (QST)
	A913/A913M Gr. 65 [450]	HSLA steel produced by quenching and self-tempering process (QST)
70 ksi (485 MPa)	A709/A709M QST 70 [QST 485]	HSLA steel produced by quenching and self-tempering process (QST)
	A913/A913M Gr. 70 [485]	HSLA steel produced by quenching and self-tempering process (QST)
80 ksi (550 MPa)	A913/A913M Gr. 80 [550]	HSLA steel produced by quenching and self-tempering process (QST)

building designs, which has, in turn, limited the production of the material (Stall et al., 2024). While high-strength steel is still more expensive on a per-ton basis, the cost premium for rolled shapes with $F_y = 65$ ksi is generally modest (5–10%), whereas for $F_y = 80$ ksi, the premium may range from 10–20%, depending on section availability, production methods, and regional market conditions (AISC, 2019; ArcelorMittal, 2020). Although high-strength steel may have a higher unit cost, its use can reduce total material tonnage and fabrication effort, leading to potential cost savings at the system level, particularly in long-span or high-rise applications.

High-strength rolled shape steel columns, particularly those specified under ASTM A572 (2021b) Grade 65 and A913 Grades 65, 70, and 80, have become increasingly viable for structural applications due to advances in QST manufacturing. These grades offer enhanced strength and comparable ductility to conventional steels, enabling potential reductions in member size, weight, and embodied carbon. However, design provisions such as those in AISC 360, *Specification for Structural Steel Buildings* (2022b), hereafter referred to as AISC 360, have not yet been recalibrated to fully reflect the unique residual stress patterns and imperfection behavior of these modern high-strength materials. While previous studies on welded and cold-formed high-strength steel (e.g., S690 plates, rectangular HSS, box sections) have contributed to understanding flexural buckling behavior in high-strength applications, those findings may not directly translate to rolled W-shape columns, where residual stress magnitudes, distributions, and geometry differ substantially. A more targeted evaluation of design curve applicability is therefore needed for high-strength rolled shapes, particularly those produced to ASTM A913 specifications.

The hot-rolled wide flange shapes that have been used in U.S. building construction to date are high-strength low-alloy (HSLA), including the use of the QST process with specified yield strengths up to 80 ksi (550 MPa). These products are readily available for supply to projects in the United States and across the world, although domestic production of rolled shapes exceeding $F_y = 65$ ksi is currently limited to a small number of producers. These products are permitted for use in steel buildings per AISC 360 (2022b), Section A3.1a (Listed Materials), and shown in Table A3.1. Hot-rolled wide-flange shapes listed in Table A3.1 with F_y values of 65 ksi (450 MPa) or greater are duplicated here in Table 1. As shown in Table 1, ASTM A913 is a quenching-and-self-tempering (QST) processed specification developed specifically for rolled structural shapes in Grades 65, 70, and 80. ASTM A572 is a general-purpose, high-strength low-alloy steel specification applicable to plates, bars, and shapes, but it does not require QST processing. ASTM A709 (2018b) is a bridge steel specification that integrates requirements from A913 or A572, depending on the grade and intended application. For instance, A709 Grade 70W (QST) corresponds to A913 Grade 70 with additional requirements for notch toughness and weldability. This study focuses exclusively on wide-flange shapes produced to ASTM A913 Grade 80.

AISC 360-22 allows the usage of the materials shown in Table 1 with a specified F_y of 65 ksi to be used without any special limits or considerations, including designing by inelastic analysis (AISC 360-22, Appendix 1). The allowable use of inelastic analysis infers these steels possess adequate static ductility when designing within the prescribed limits of AISC 360, including utilizing limits on cross-sectional geometrical limits and component slenderness.

For materials listed in AISC 360-22 with a specified yield stress greater than 65 ksi (in Table 1, this would include A913/A913M Gr. 70 and Gr. 80 material), there are both explicit prescribed limitations when using these materials (such as prohibition to use them if plastic hinging is

expected based on inelastic analysis per Appendix 1, Section 1.3.2a) and design rules that likely do not apply to these materials in the same way as lower strength materials. However, major evidence exists that current design rules (e.g., AISC 360-22, Eurocode 3, Part 1-1) are likely overly conservative for these high-strength steels when employed as structural steel columns, due in part to assumptions regarding residual stresses (Ban et al., 2013; Shi et al., 2012; Li et al., 2016; Stroetmann and Penner, 2024).

The column design curve adopted in Eurocode 3, Part 1-1 (CEN, 2005a), are based on the Perry-Robertson formulation, with calibration performed using an extensive experimental database assembled by the European Convention for Constructional Steelwork (ECCS). The curve families (designated by imperfection factors α) reflect the effect of geometric imperfections and residual stresses across different cross-section types. These include cold-formed, hot-rolled, and built-up shapes, with the choice of α determined by member type and fabrication method. Based on these conditions, Eurocode 3 (EC3) provides a family of five column buckling curves (a_0, a, b, c, d), with each curve tailored to different residual stress distributions, imperfection sensitivities, and section types. Curve a_0, for example, reflects high-quality hot-rolled sections with low imperfection amplitudes, while curves c and d are reserved for fabricated or cold-formed members more prone to geometric variability. This multiplicity of curves allows Eurocode 3 to better reflect the diverse behaviors of different steel column types.

In contrast, AISC 360, Chapter E, adopted a single unified column design curve for simplicity and conservatism, which was developed based on calibration studies primarily using mild steel grades such as ASTM A36 (2019a) and A572 Grade 50. These calibrations—originally developed through the Structural Stability Research Council (SSRC) and summarized in its *Guide to Stability Design Criteria for Metal Structures* (Galambos, 1998)—assumed idealized residual stress patterns (e.g., $\pm 0.3F_y$ for flanges and webs) and geometric imperfections representative of conventional rolling and fabrication processes from the 1960s to 1980s. The development of this column curve is based on assumptions regarding initial out-of-straightness and residual stress distributions, as outlined in Appendix 1 of AISC 360. However, modern high-strength rolled shapes (e.g., A913 Grade 80) produced by QST processes tend to exhibit reduced residual stress magnitudes (relative to F_y) and more uniform geometric tolerances due to tighter production controls. As a result, application of the existing AISC curve—originally intended as a single conservative envelope—may be overly restrictive for such shapes, especially in the inelastic slenderness range where residual stresses and geometric imperfections play a dominant role. In this study, the validity of these assumptions is assessed for high-strength rolled W-shape columns by explicitly modeling residual stress distributions and initial imperfections in finite element (FE) simulations. The resulting buckling strengths are then compared to those predicted by Chapter E to evaluate whether the current design curve remains appropriate for A913 Gr. 80 shapes, or if modification may be warranted.

The primary objective of this study is to investigate the flexural buckling behavior of wide-flange rolled steel columns fabricated from both conventional mild steel [ASTM A992 (2020), $F_y = 50$ ksi] and high-strength structural steel (ASTM A913 Grade 80, $F_y = 80$ ksi). Finite element models are developed to incorporate validated residual stress distributions, initial geometric imperfections, and nonlinear material behavior. The simulated minor and major axis buckling responses are used to evaluate the accuracy and applicability of the current AISC 360-22 column design provisions across a range of cross-sectional geometries and slenderness ratios. The inclusion of A992 serves as a reference baseline to benchmark current design performance, while the comparison to A913 Gr. 80 highlights potential deviations that may warrant refinement of existing design curves for high-strength rolled W-shape columns. As mentioned before, AISC 360 and Eurocode 3 design column curves are rooted in decades of experimental and analytical research and are the result of rigorous reliability-based calibration procedures (e.g., the SSRC Column Curves for AISC and Perry-Robertson-based methods for EC3). These were based on extensive databases covering a wide range of geometries, materials, and imperfections, providing statistically defensible strength predictions across broad design applications. The current study does not attempt to replicate this statistical calibration effort but, instead, uses validated finite element simulations to assess how the EC3 and AISC 360 curves compare when applied to A913 Gr. 80 (F_y = 80 ksi) wide-flange sections.

PRIOR RESEARCH ON HIGH-STRENGTH STEEL

Numerous experimental and numerical studies have examined the flexural buckling behavior of high-strength steel members. Much of the prior work has focused on built-up or welded sections fabricated from plate products such as S690 ($F_y = 690$ MPa or 100 ksi) steel, which can exhibit different residual stress profiles and imperfection sensitivities compared to rolled shapes. Studies have also investigated cold-formed hollow structural sections (HSS), including square and rectangular tubes formed from high-strength strip steel. These sections often behave differently due to the cold-forming process and are governed by different design provisions.

Rasmussen and Hancock (1995) investigated the flexural buckling capacity of 12 welded H-sections and 13 box sections with yield strengths of 100 ksi and higher. They found that the Australian, American, and British standards

were conservative, and they suggested using buckling curve *a* instead of curve *c* in European standards for minor axis buckling when using HS3. Li et al. (2012) conducted 12 tests on welded box and H-sections and confirmed that buckling curve *a* is more accurate than curve *c* in European standards, and certain European buckling curves may be overly conservative for high-strength steel columns. Ban et al. (2013) tested six welded box and H-sections made from 140 ksi steel, evaluating their buckling behavior and suggesting modifications to existing design curves. They recommended buckling curve *a* in European standards for these columns. In addition, their study suggested a revised imperfection factor for European standards with further validation. Khan et al. (2013) investigated 15 welded box sections, focusing on composite columns, and recommended using buckling curve *a* in European standards for composite high-strength steel and high-strength concrete (HSC) sections. Wang and Gardner (2013) tested eight hot-finished rectangular HSS columns with yield strength of 100 ksi and recommended using AISC 360 as-is or Eurocode 3, Part 1-1, with some modifications. Ma et al. (2015) investigated welded H-sections made from S690 steel, assessing the applicability of existing design standards to slender columns. Their study concluded that Eurocode 3, Part 1-1, underestimates buckling resistance and AISC 360 better matches actual failure loads. Somodi and Kövesdi (2016, 2017) studied the flexural buckling behavior of 12 cold-formed rectangular HSS columns made of 100 and 140 ksi steels. Their study suggested that curve *b* in European standards should be used for columns made of 70–100 ksi steel and curve *a* should be used for 140 ksi steel columns. Additional tests on six welded box-sections indicated that curve *c* is conservative, recommending curve *a* for 70–140 ksi steel columns.

More recently, Sun et al. (2020), presented experimental and numerical studies on the flexural buckling of S690 high-strength steel welded I-section columns. Comparisons with European (Eurocode 3, Part 1-2), American [ANSI/AISC 360 (2016)], and Australian [AS 4100 (2020)] standards showed that Eurocode 3, Part 1-2 (CEN, 2005b) and AS 4100 were overly conservative in predicting buckling resistance, whereas AISC 360-16 provided reasonable predictions, but with some overestimated resistances for intermediate and long columns. The authors proposed an improved design approach that modifies the EC3 buckling curve, leading to safer and more accurate resistance predictions. Ferreira Filho et al. (2022) studied the flexural buckling resistance of S690 high-strength steel welded I-section columns and beam-columns. The research includes experimental testing, numerical modeling, and an evaluation of current design standards (Eurocode 3, AISC 360, AS 4100). The results of the study indicated that EC3 was overly conservative, underestimating buckling resistance, whereas AISC 360 was more accurate but slightly overestimated resistance in some cases. AS 4100 results were also conservative, similar to Eurocode 3. Hence, the authors proposed a revision of buckling curves in EC3 to better reflect welded I-section column behavior.

Yun et al. (2023) investigated the flexural buckling behavior of homogeneous and hybrid welded I-section columns across a range of steel grades (S235 to S960). The research includes residual stress analysis, experimental testing, finite element modeling (FEM), and evaluation of current design standards. Eurocode 3, Part 1-1 (CEN, 2005a), and AISC 360 were assessed. The results from the study demonstrated that EC3 was too conservative for high-strength steels, underestimating buckling resistance, whereas AISC 360 performed better but was inconsistent for lower steel grades. Based on the responses, the study suggested revising EC3 buckling curves to reflect the effect of steel grade on buckling resistances, which improved accuracy and consistency. Stroetmann and Penner (2024) investigated the buckling resistance and residual stress distributions in welded box columns made from high-strength steel (S460 to S960). The research aims to reassess EC3 (CEN, 2005a, 2005b) buckling curves for HSS columns. It was observed that current EC3 underestimates buckling resistance for high-strength steel columns, and hence, the study suggested revision of buckling curves for welded box sections in EC3. These findings indicate that current design standards (AISC 360, EC3) for HS3 flexural buckling may be overly conservative as indicated in Figure 1 and may need revision to prevent overly conservative and uneconomical designs.

In Figure 1, the critical buckling strength is normalized by the yield stress, F_{cr}/F_y and plotted in the vertical axis, and the nondimensional slenderness ratio λ is plotted in the horizontal axis, which is given by Equation 1 as follows:

$$\lambda = \frac{1}{\pi}\frac{L_c}{r}\sqrt{\frac{F_y}{E}} \tag{1}$$

In this plot, comparisons are made among the experimental responses, AISC 360, and EC3 high-strength column buckling curves. This figure clearly demonstrates that the column buckling strengths predicted from the design standards are overly conservative. The EC3 column buckling curve *a* is comparable with the AISC 360 column curve, and EC3 column buckling curve a_0 is showing the most reasonable prediction of the experimental buckling strengths. Note that the addition of curve a_0 in EC3 was done because it was noted that relatively higher-strength steels are generally used in tubular profiles, resulting in higher resistances (Beer and Schulz, 1975). As a result, it is anticipated that the a_0 curve will represent the experimental responses better than the other EC3 curves. Also note that most of the experimental data plotted in Figure 1 are based on tests on

welded H, I, and box sections that may not behave similar to rolled shapes. While valuable in understanding the broader behavior of high-strength steel columns, the findings from these prior studies may not be directly transferable to hot-rolled W-shape columns produced via QST. Therefore, while it is important to acknowledge the broader literature on high-strength steel members, the present study focuses specifically on rolled W-shape sections produced to ASTM A913 standards (Grade 80), where residual stress distributions, material hardening, and geometric imperfections differ substantially from built-up or cold-formed sections.

FINITE ELEMENT MODELING

Three-dimensional (3D) nonlinear finite element models are developed for wide-flange rolled-shape columns using the finite element analysis (FEA) software ANSYS (ANSYS, 2023). The finite element models include geometric and material nonlinearities. The simply supported columns are modeled and discretized by 20-noded solid brick elements (SOLID 186). It is defined by 20 nodes having three degrees of freedom at each node: translations in the nodal x, y, and z directions. This type of element has plasticity, hyperelasticity, stress stiffening, creep, large deflection, and large strain capabilities. A typical finite element mesh of a column along with the boundary conditions for simulating major and minor axis buckling is shown in Figure 2. The fillet present in the rolled shapes is not modeled and the cross-sectional area, moment of inertia, and radius of gyration are calculated without consideration of the fillets. The x-axis corresponds to the longitudinal column axis, and the y- and z-axes are in the plane of the cross section. The y-axis is parallel to the web, and the z-axis is parallel to the flanges. All the column configurations for

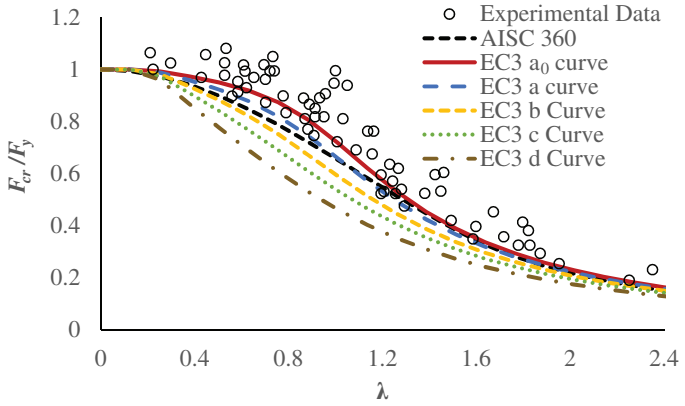

Fig. 1. Comparison of the experimental results (Rasmussen and Hancock, 1995; Li et al., 2012; Ban et al., 2013; Khan et al., 2013; Wang and Gardner, 2013; Ma et al., 2015; and Somodi and Kövesdi, 2016, 2017) on HS3 columns and the normalized flexural buckling curves.

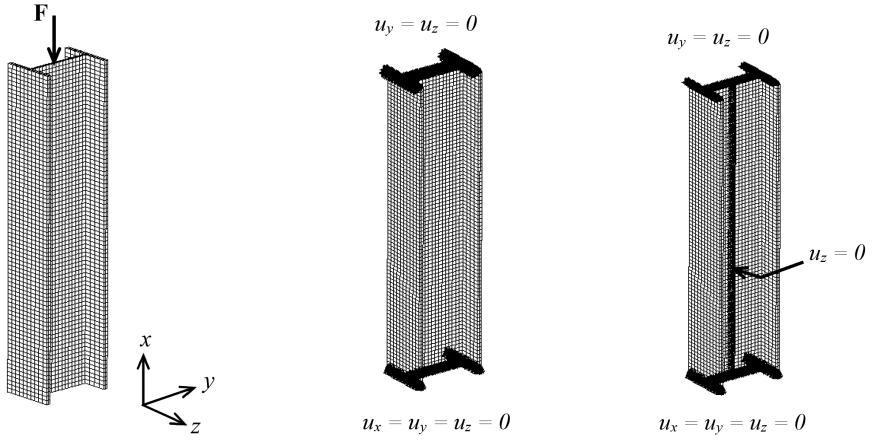

(a) FE mesh *(b) Minor axis buckling* *(c) Major axis buckling*

Fig. 2. A typical finite element mesh of a wide flange column with boundary conditions for minor and major axis buckling.

the present investigation are simply supported. The column is pin-supported at the bottom, and the same boundary condition is applied at the top with the exception that vertical translation is permitted [Figures 2(b) and 2(c)]. For major axis buckling, the column is restrained against minor axis deflections by translational supports along the length as shown in Figure 2(c).

Material Model

In the finite element modeling of columns, it is important to use the characteristic yield stress related to the grade of steel and the shape of the material stress-strain curve. It has been demonstrated that the yield plateau and strain hardening have an influence on short columns with low slenderness (Snijder et al., 2014; Jönsson and Stan, 2017); however, for slender columns, no significant difference is seen, with respect to differences in strain hardening or having a yield plateau (Moghadam, 2015; Jönsson and Stan, 2017). Most of the studies in the literature demonstrated that an elastic-perfectly plastic material model can reasonably provide the code-specified column buckling responses (Snijderet al., 2014).). In this study, column buckling responses are investigated for ASTM A992 steel and A913/A913M Gr. 80 high-strength steel to understand the applicability of AISC 360-22 column curves in predicting the column buckling strength. The nonlinear material properties of ASTM A992 steel and A913/A913M Gr. 80 structural steel in ANSYS are incorporated using the multilinear kinematic hardening model with the initial elastic modulus, Poisson's ratio, and stress-strain data obtained from the uniaxial tension tests.

The multilinear kinematic hardening model is a rate-independent plasticity model that accounts for the effect of plastic deformation on the Bauschinger effect (Bauschinger, 1886). The constitutive equations are based on a von Mises yield function, associated flow rule, and a kinematic hardening rule. An overview of the multilinear kinematic hardening model is given below to show different features of the model. The yielding is determined by von Mises criterion:

$$f(\underline{\sigma}-\underline{\alpha})=\left[\frac{3}{2}(\underline{s}-\underline{a})(\underline{s}-\underline{a})\right]^{1/2}=\sigma_0 \tag{2}$$

where $\underline{\sigma}$ is the stress tensor, $\underline{\alpha}$ is the current center of the yield surface in the total stress space, $\underline{s}$ is the deviatoric stress tensor, $\underline{a}$ is the current yield surface center in the deviatoric space, and σ_0 is the initial size of the yield surface. The associated flow rule is used to calculate the rate-independent plastic strain increments:

$$d\underline{\varepsilon}^p=d\lambda\frac{\partial f}{\partial\underline{\sigma}}=\frac{3}{2}dp\frac{\underline{s}-\underline{a}}{\sigma_0} \tag{3}$$

The kinematic hardening rule is based on backstress evolution, which defines the translation of the yield surface. The general form is as follows:

$$d\underline{a}=\frac{2}{3}Cd\underline{\varepsilon}^p-\gamma\underline{a}dp \tag{4}$$

where C is the initial kinematic hardening modulus, γ is hardening parameter that controls how backstress saturates, and dp is the plastic strain rate. The multilinear approach approximates nonlinear hardening behavior using piecewise linear segments, instead of using a smooth curve. The total backstress is computed as:

$$d\underline{a}=\sum_{i=1}^{n}d\underline{a}_i \tag{5}$$

where each $\underline{a}_i$ follows a linear hardening rule with its own modulus.

The uniaxial tension test data for ASTM A992 was obtained from the tests performed by Morrison (2015) as shown in Figure 3(a) along with the fitted multilinear model in engineering stress-strain format for consistency with the original test data. However, for numerical implementation in ANSYS, the experimental data were converted to true stress-true plastic strain, which is the required input format for the multilinear kinematic hardening model. Similar to other conventional mild steel, A992 steel exhibited a yield plateau with a longer strain-hardening region and higher ductility. Additionally, it is important to note that the multilinear plasticity models in ANSYS Mechanical APDL do not accept negative slopes in the stress-strain input data. That is, the input curve must be nondecreasing in stress with respect to strain. For this reason, material softening cannot be captured directly in this model. As a result, the plasticity curves were truncated prior to the onset of instability and localization.

In the multilinear model, the elastic modulus of A992 steel is taken as 29,000 ksi with yield stress and tensile strength of 50 and 67 ksi, respectively. Data from five uniaxial tension test coupons performed by a producer of A913/A913M Gr. 80 hot-rolled, wide-flange shapes were provided for the current study. The stress-strain data is presented in Figure 3(b) with the fitted multilinear model used in the simulations as well as the elastic-perfectly plastic (EPP) model for comparison. It is observed that A913/A913M Gr. 80 material does not exhibit a yield plateau, and hence, the 0.2% offset method is used to calculate the yield stress of each coupon which, was found to be close to 80 ksi on average. The modulus of elasticity was comparable among the five tests performed, which is taken as 29,000 ksi in the multilinear model. The strain-hardening region is very small, demonstrating a lower ductility. Similar observations were made in the study performed by Stall et al. (2024) for ASTM A656/A656M (2018a) Gr. 80 steel.

Modeling of Initial Imperfection

Von Kármán (1907) identified out-of-straightness and out-of-plumbness as the most critical global imperfections affecting column buckling. Modern standards, including Eurocode 3, Part 1-1 (CEN, 2005a), and AISC 360-22, set limits on these imperfections, with Eurocode 3 being more conservative. The out-of-straightness imperfection amplitude of $L/1500$ was adopted for the AISC 360 standard (Tide, 2001) for developing the column buckling curves, which is close to the average value determined statistically by Bjorhovde (1972), whereas Eurocode 3 adopted $L/1000$ as the out-of-straightness imperfection value (Beer and Schulz, 1975; Strating and Vos, 1975). These standardized values were established based on research conducted between the 1960s and 1980s in the United States, Europe, and Japan. Experimental studies by Fukumoto and Itoh (1983) showed that the maximum out-of-straightness imperfection is usually exhibited by the IPE160 sections, which is in the range of $L/1000$, while hot-rolled tubular and welded wide-flange sections had smaller out-of-roundness imperfections, leading to better buckling performance. As a result, the assumption of $L/1000$ initial imperfection for all the available column sections is an overly conservative approach of including the out-of-straightness in the buckling strength calculation in Eurocode 3. Note that the unified column curve in AISC 360-22 is based on SSRC Column Curve, 2P, which assumes an initial out-of-straightness of $L/1500$ for analytical purposes. However, it is important to note that AISC 360 itself does not prescribe fabrication or erection tolerances. Actual tolerances for out-of-straightness and out-of-plumbness are governed by AISC 303, *Code of Standard Practice* (2022a), which references applicable ASTM standards in Section 11.2.2.1. For wide-flange rolled shapes, these standards typically specify a fabrication tolerance of approximately $L/1000$, indicating that the imperfections used in the design curve derivation are slightly more severe than typical fabrication practice.

Beyond global imperfections, local imperfections arise due to fabrication processes, with their shape and amplitude varying by manufacturing method. While these imperfections were not directly studied in buckling experiments, their effects on flexural buckling resistance were included in statistical analyses alongside factors like boundary conditions, out-of-plumbness, and material properties (Bjorhovde, 1972; Fukumoto and Itoh, 1983).

For nonlinear buckling analysis to be accurate using finite element simulation, it is necessary to set an initial imperfection in the column being modeled along with the residual stress distribution. The shape of the geometric imperfection is based on the buckling mode belonging to the lowest eigenvalue from a linear buckling analysis. This usually results in a sinusoidal bow imperfection. The amplitude defining the maximum deviation from the ideal geometry is taken as $L/1500$ as used in AISC 360 for buckling simulation of the columns. The imperfections of the finite element model are established by first performing a linear buckling analysis on the perfect prismatic column model with given boundary conditions, then the relevant (displacement) normalized global buckling mode is extracted. In the following nonlinear FE calculations, the imperfections are established by importing the normalized displacements of the lowest global buckling mode in the relevant plane of buckling as shown in Figure 4, multiplying this by the maximum imperfection magnitudes and updating the nodal coordinates of the model by adding the established nodal imperfections.

Modeling of Residual Stresses

Structural steel members develop residual stresses due to manufacturing and fabrication processes. Depending on size and welding procedure, the magnitude and distribution of these residual stresses can vary significantly in members. Hence, it is challenging to accurately predict the magnitude

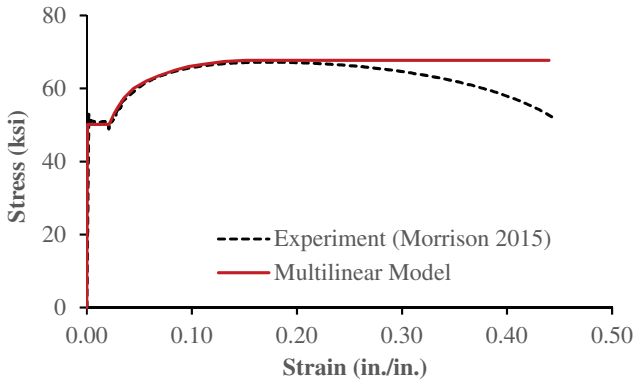

(a) ASTM A992 steel (data from Morrison, 2015).

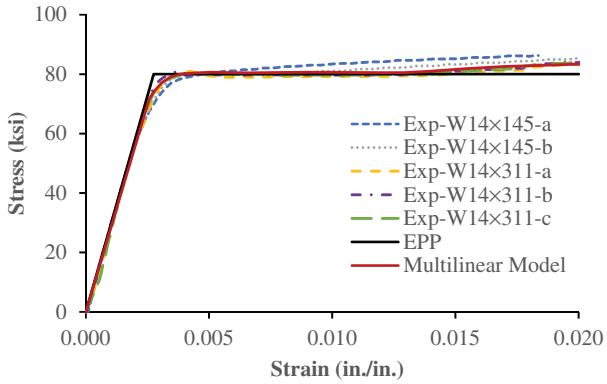

(b) A913/A913M Gr. 80 steel (producer supplied data).

Fig. 3. Uniaxial tension test data along with the fitted material models in engineering stress-strain format.

and distribution of residual stresses in steel structural members, which can substantially affect their structural performances, including global and local flange-buckling strengths, seismic performances, and low-cycle fatigue responses. Residual stresses are either ignored or a simplified distribution is assumed in the analysis and design of structural members. Literature suggests that the presence of residual stresses can influence the sensitivity of beam design curve (Rossi et al., 2021) in the intermediate length range and can be crucial for structural steel columns and welded connections (Huber, 1956; Lamarche and Tremblay, 2011; Mathur et al., 2012). The monotonic buckling strength and cyclic strength degradation of columns in a structural steel frame are substantially influenced by the initial residual stresses (IRSs) (Lamarche and Tremblay, 2011; Mathur et al., 2012).

Previous studies on the nonlinear buckling analysis of steel columns showed that the simplified linearized distribution of residual stresses yielded conservative results. However, most of the residual stress distribution for the rolled shapes available in the literature was developed in the 1970s based on ASTM A36 steel, and it is warranted that residual stresses be measured for high-strength steel rolled shapes. Jönsson and Stan (2017) pointed out that if the magnitude of residual stresses is wrongly assumed to be proportional to the yield stress, the column buckling capacity of steel columns found by finite element analysis will be underestimated for higher grades steel. A study by Boissonnade and Somja (2012) also demonstrated that placing different steel grades on the same buckling curve leads to an overly conservative design for high-strength steels. Hence, in this study, the multiaxial residual stress distribution in the rolled shapes considered in the analysis is developed by using a sequentially coupled thermomechanical analysis as presented in Quayyum and Hassan (2017). This computational scheme was validated against four W-sections using A36 steel (Quayyum and Hassan, 2017). In this study, the column buckling capacities are investigated for A992 and A913/A913M Gr. 80 steels. Hence, it is important to understand the accuracy of the computational scheme in predicting the magnitude and distribution of residual stresses in W-shapes using these steels.

The numerical scheme for residual stress simulation assumes that during the manufacturing of W-shapes, residual stress distribution observed in a W-shape primarily develops during the cooling process after hot rolling (Alpsten, 1968). Hence, this study simulated only the evolution of residual stresses during the cooling process. In cooling process simulation, the real-time temperature field in W-shapes during cooling after hot-rolling is calculated first by employing heat transfer analyses. The temperature field at each step of the heat transfer analysis is stored and used as an input in the residual stress analysis for calculating the evolution of stress and strain fields in the W-shapes during the cooling process—that is, the heat transfer analysis is sequentially coupled with thermomechanical residual stress analysis. The link between the heat transfer analysis and stress analysis is obtained through the temperature history, which is input as the thermal load in the residual stress analysis.

In the thermal analysis, the finite element models of the W shapes are discretized by 20-noded solid thermal elements (SOLID279). These elements have temperature as one degree of freedom at each node. The W-shapes are initially heated to a uniform temperature of 1300ºC, which is kept constant for 10 min before starting the air cooling. The

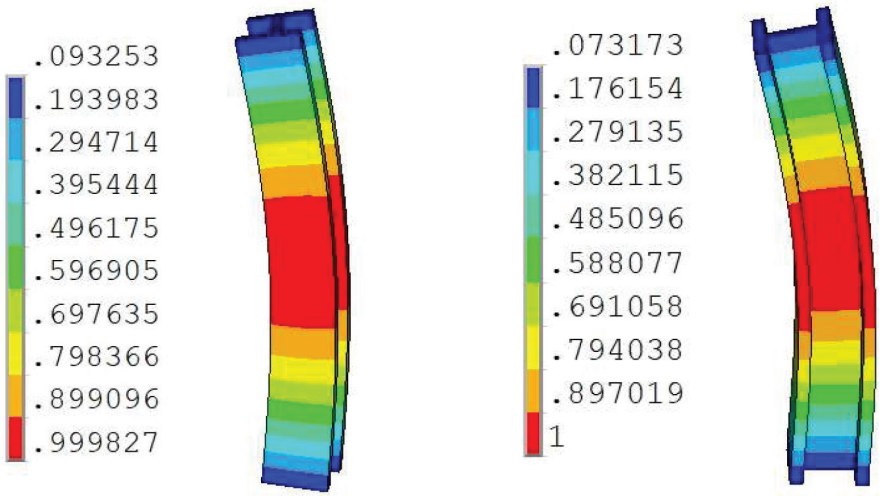

(a) Minor axis *(b) Major axis*

Fig. 4. Normalized displacements of the lowest global buckling mode from elastic buckling analysis.

air cooling is simulated in thermal analysis by using a heat transfer coefficient, which includes convection, conduction, and radiation into the air. The material is considered homogeneous and isotropic throughout the cross section, and the material coefficients such as specific heat, thermal conductivity, and heat transfer coefficient are defined as a function of temperature. The simulation of the heat transfer from the surface of the W-shapes largely depended on the heat transfer coefficient, which includes the effect of convection, conduction, and radiation. The density of the material is assumed constant. Enthalpy of the material is defined as a function of temperature in order to account for the phase transformation (Comini et al., 1974). In the thermal finite element analysis, a uniform temperature of 25°C is assigned to all nodes as the initial boundary condition and the reference temperature for thermal strain calculations. At each time step, heat transfer is applied to each node of the solid model surface, and then the solid model surface loads are transferred to finite element model. At each time step, the material properties are assigned as a function of nodal temperature. The temperature distribution of a W12×87 section is presented in Figure 5 at different stages of the cooling process.

This shows that the W-shapes are not uniformly cooled; the cooling is faster at the edges of the beam and at the mid-depth of the beam web compared to the flange-web junction area. The cooling rate is slightly reduced when the phase transformation temperature (650°–760°C) has been reached, owing to phase transformation heat. After the phase transformation region, the cooling rate increases almost to the rate at the inception of phase transformation and continued cooling with progressively reduced rates to reach the room temperature.

The residual stress analysis uses the temperature history from the thermal analyses as an input. The nodal temperature history at each of these steps shall be considered thermal load for the corresponding node from a structural model in this analysis. Therefore, it is necessary to match the number of meshes and nodes for stress analysis with those applied in a temperature analysis. This is accomplished by changing the element types from thermal solids (SOLID279) to structural solids (SOLID186) by using the ETCHG command available in ANSYS. For the constitutive model chosen, the temperature-dependent material properties for structural steel are required for the residual stress analysis. Note that material and geometrical nonlinearities are incorporated into the residual stress computation. The essential material properties required in the analysis are density, initial yield stress, elastic modulus, Poisson's ratio, and thermal expansion coefficient. It is assumed that the density remains constant while the other material properties are dependent on the temperature. The initial yield stress, the elastic modulus, and the multilinear kinematic hardening model parameters are determined from the monotonic stress-strain responses of ASTM A992 steel at various temperatures obtained from Hu et al. (2009) as shown in Figure 6. For details of the material properties and model parameters, the readers are referred to Quayyum and Hassan (2017).

In the thermomechanical analysis, 25ºC is considered as the reference temperature for thermal strain calculations, and the nodal temperatures at each time step from the thermal analysis are read to calculate the corresponding stresses and strains at the time step by using the temperature-dependent structural material properties of steel. The simulated residual stress contours for a W12×87

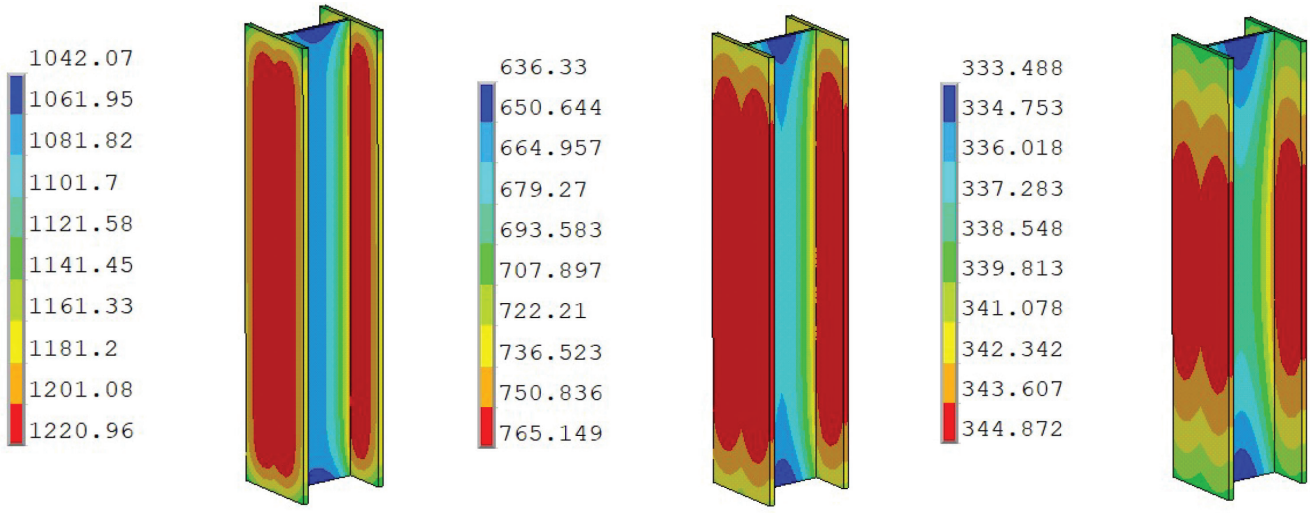

(a) 15 minutes *(b) 45 minutes* *(c) 105 minutes*

Fig. 5. Temperature distribution (in K) during cooling of W12×87 section from initial 1300°C reheat temperature.

section is plotted in Figure 7 at different stages of cooling. It is observed that the residual stresses are initially tensile in the web that turns compressive with the progression of cooling. On the other hand, the residual stresses are initially compressive in the flange-web junction but turn tensile with the progression of cooling. The residual stresses stabilized after 2 hr of cooling. The simulated residual stresses after cooling to ambient temperature at the beam mid-length are compared to the measured values from Lamarche and Tremblay (2011) in Figure 8. The simulation results show that the computation scheme is able to predict the residual stresses in the web and flanges of W12×87 section with good accuracy. This further validates that the computational scheme previously validated for A36 steel can also be applicable to determine the residual stresses in W-shapes with A992 steel. The residual stresses predicted by the model proposed by Galambos and Ketter (1959) are also plotted in Figure 8 for comparison purposes. It is observed that the flange and web stresses are underpredicted by the Galambos and Ketter model (1959). Note that the web stress is assumed tensile in the Galambos and Ketter (1959) model, whereas the measured stress in the web is both tensile and compressive. This is also true for many other shapes (Fujita, 1955; Huber, 1956; Alpsten, 1968). Based on this observation, this study considered residual stress distribution obtained from the finite element simulation as the initial stress state in the wide flange column shapes for buckling strength calculations.

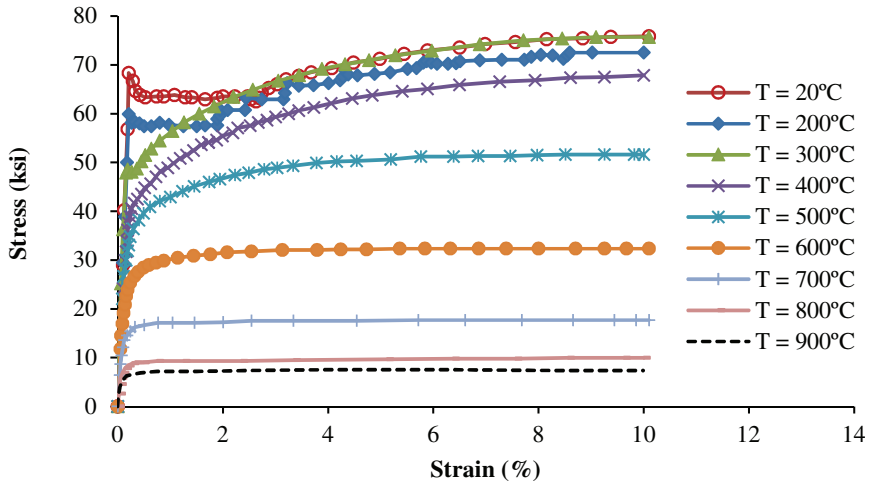

Fig. 6. Monotonic stress-strain response of ASTM A992 steel at various temperatures (Hu et al., 2009).

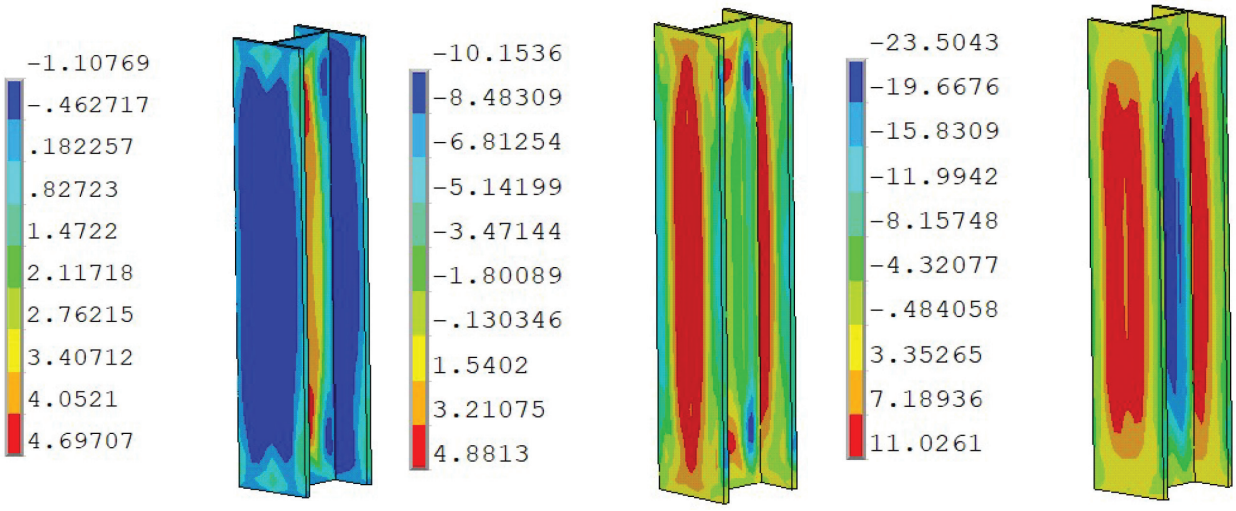

(a) 15 minutes *(b) 45 minutes* *(c) 2 hours*

Fig. 7. Longitudinal stress contour (in ksi) of hot-rolled W12×87 section at various instances after the start of cooling.

In order to investigate whether the computational scheme can predict the residual stresses in rolled wide-flange shapes made of A913/A913M Gr. 80 steel, the experimental data from Spoorenberg et al. (2013) is obtained for a W14×808 quenched and self-tempered (QST) section. This section is provided by ArcelorMittal (2020) with a yield stress around 80 ksi, and the residual stresses were measured by the sectioning method. The computational scheme as discussed earlier is used to simulate the residual stresses in a W14×808 section. However, material properties of A913/A913M Gr. 80 steel are not available for elevated temperatures. As a result, the thermal material properties, such as specific heat, thermal conductivity, enthalpy, and heat transfer coefficient, and some of the structural material properties, such as Poisson's ratio, density, and thermal expansion coefficient of A913/A913M Gr. 80 steel, are considered the same as used in the simulation of A992 steel. On the other hand, the elastic modulus and the stress-strain data for 80 ksi steel are obtained from the study performed by Huang et al. (2018) as shown in Figure 9, where they investigated the elevated temperature material properties of Chinese Q550 steel.

These stress-strain data were fitted with a multilinear model to incorporate the nonlinear material properties in the simulation at different temperatures. Similar to W12×87 consisting of A992 steel, it is observed that the residual stresses in W14×808 are initially tensile in the center of the web, which turns compressive with the progression of

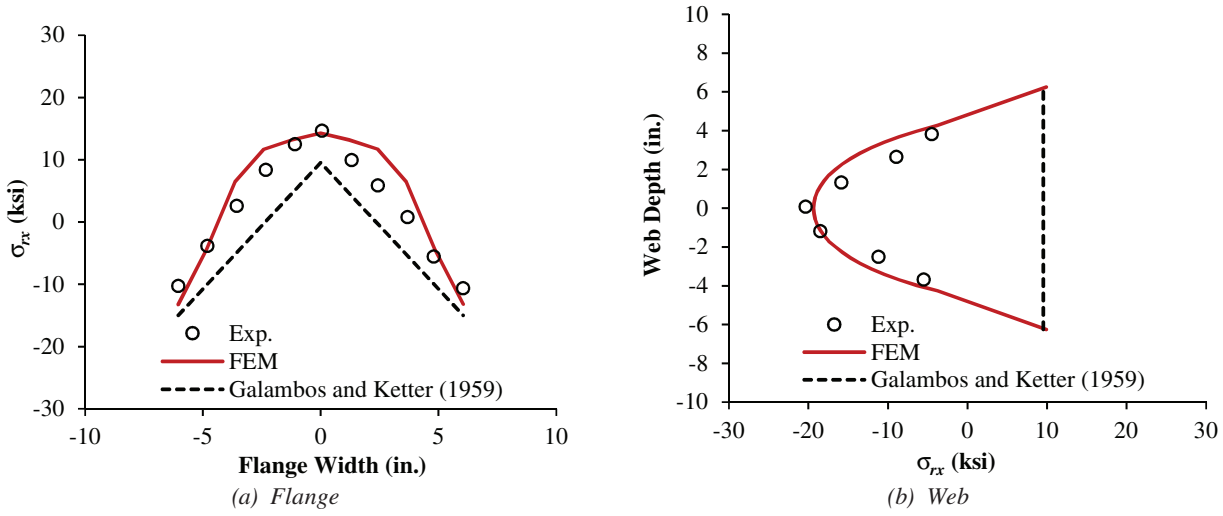

(a) Flange *(b) Web*

Fig. 8. Comparison of FEM and analytical simulations to measured IRSs in the flange and web of ASTM A992 W12×87 beam section (data from Lamarche and Tremblay, 2011).

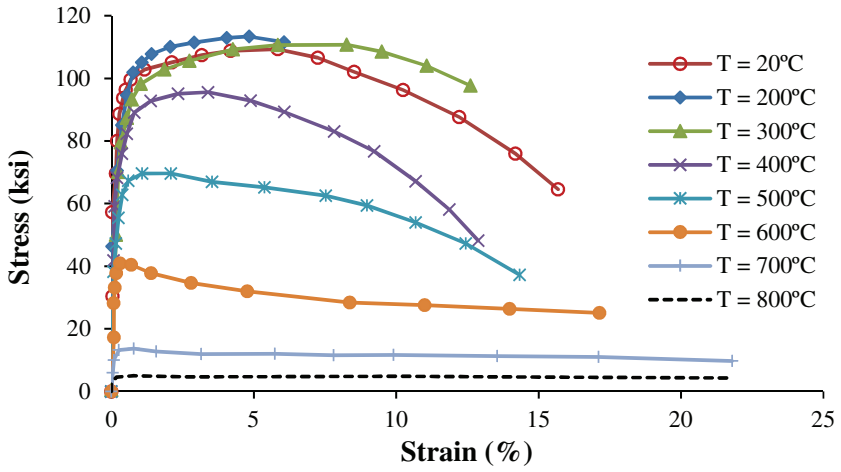

Fig. 9. Monotonic stress-strain response of Q550 steel at various temperatures (Huang et al., 2018).

cooling. On the other hand, the residual stresses are initially compressive in the flange-web junction, which turns tensile with the progression of cooling. Because of thicker flanges, the residual stresses stabilized almost after 12 hr of cooling. The simulated residual stresses after cooling to ambient temperature at the beam mid-length are compared to the measured values from Spoorenberg et al. (2013) in Figure 10 along with a comparison with the Galambos and Ketter (1959) model. The simulation results show good agreement with the measured values; hence, in the simulation of the buckling curves for rolled W-shapes using A913/A913M Gr. 80 material, the simulated residual stress distribution is considered for the rest of the analysis in this study. Note that the prediction of the residual stress in the flanges using the Galambos and Ketter (1959) model is also in good agreement with the measured values; however, the web stress is not predicted well by the Galambos and Ketter model. As mentioned before, the web stress is entirely considered as tensile stress in Galambos and Ketter (1959) model, whereas measured values show the presence of both tensile and compressive stresses in the web.

VALIDATION OF THE FINITE ELEMENT MODEL

The FEM simulated residual stress of W12×87 section shown in Figure 7 is used in the finite element buckling analysis of a column with a 12 ft 2 in. length under displacement-controlled monotonic axial compression. The initial residual stresses are considered as the initial stress state of the column, and the nodal coordinates of the model are updated by adding the established nodal imperfections from elastic buckling analysis. Figure 11(a) shows the global buckling of column about its minor axis from the analysis considering the presence of the simulated residual stresses. Note in Figure 11 that when residual stress is included in the analysis, the initiation of global buckling occurs similarly as in the experiment (Lamarche and Tremblay, 2011), whereas, without residual stress the column remains elastic until buckling initiates. Moreover, simulated responses show local buckling at the mid-height of the column which was also observed during the experiment as shown in Figure 12 (Lamarche and Tremblay, 2011).

Consequently, simulated responses of axial load versus axial displacement [Figure 13(a)] and axial load versus lateral deflection [Figure 13(b)] are compared well to the experimental responses (from Lamarche and Tremblay, 2011) when residual stress is included in the analysis. These results demonstrate the excellent simulation of the buckling strength if FEM simulated multiaxial residual stress is included in the analysis, and overprediction of about 10% is obtained if residual stress is not included in the analysis. Once the global buckling is initiated, the lateral deflection gradually increases, and the axial load decreases with the increase in axial displacement. The post-buckling responses with or without residual stress, however, are very similar to the experimental responses, especially when lateral deflection becomes large [Figures 13(a) and 13(b)]. The validation of the numerical scheme indicates that the finite element modeling techniques described earlier can be utilized further to develop column flexural buckling curves for rolled shapes using A992 and A913/A913M Gr. 80 steels. An important modeling simplification in this study

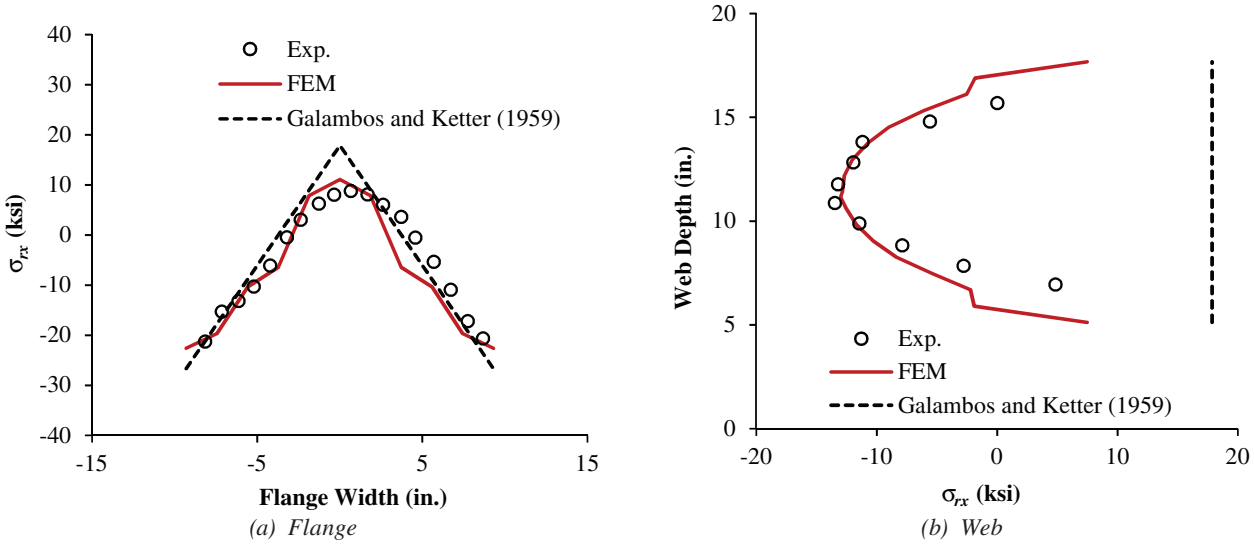

(a) Flange *(b) Web*

Fig. 10. Comparison of FEM and analytical simulations to measured IRSs in the flange and web of 80 ksi W14×808 beam section (data from Spoorenberg et al., 2013).

(a) Experimental response

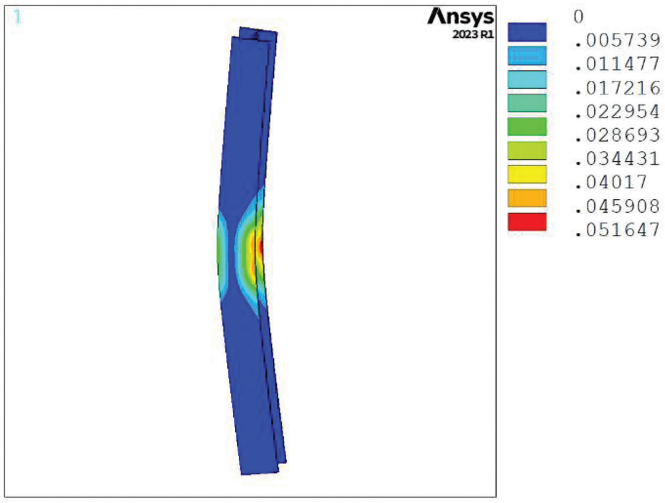

(b) Simulated von Mises plastic strain contour

Fig. 11. Experimental (from Lamarche and Tremblay, 2011) and simulated global buckling of W12×87 *shape about minor axis under monotonic axial compression.*

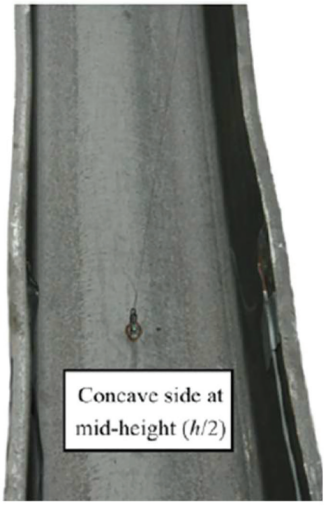

(a) Esperimental response

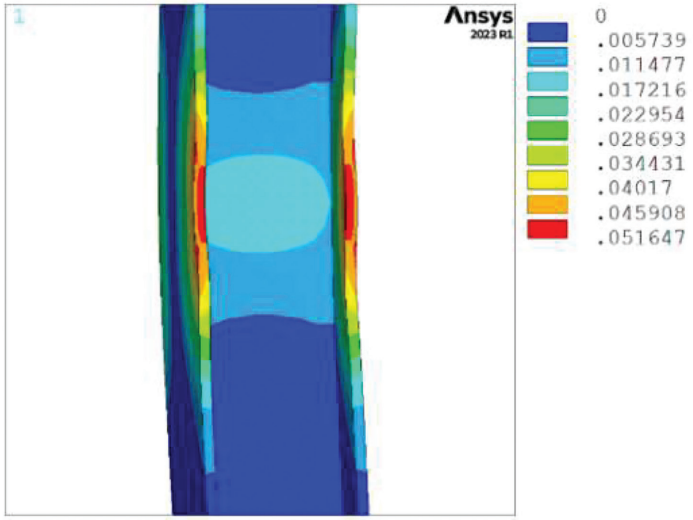

(b) Simulated von Mises plastic strain contour

Fig. 12. Experimental (from Lamarche and Tremblay, 2011) and simulated flange local buckling at the mid-height of W12×87 *shape under monotonic axial compression.*

Table 2. Cross-Sectional Properties of the W-Shapes Investigated for Column Flexural Buckling Using A992 Steel						
					Analysis Performed	
Column Designation	h/b	t_f (in.)	$b_f/2t_f$	h/t_w	Minor Axis	Major Axis
W14×808	1.23	5.12	1.82	3.04	x	
W14×605	1.20	4.16	2.09	4.39	x	
W12×336	1.25	2.96	2.26	5.47	x	x
W14×426	1.12	3.04	2.75	6.08	x	x
W14×257	1.03	1.89	4.23	9.71	x	
W14×193	0.99	1.44	5.45	12.8	x	x
W14×145	0.96	1.09	7.11	16.8	x	x
W12×87	1.03	0.81	7.48	18.9	x	x
W14×82	1.42	0.855	5.92	22.4	x	x
W14×53	1.71	0.66	6.11	30.9	x	

is the omission of the k-area (fillet region between flange and web) in the finite element geometry. While this simplification could influence the local residual stress distribution, especially in thick or heavy sections subjected to minor axis loading, its impact was evaluated by comparing simulation results to measured residual stress patterns and buckling behavior. Specifically, the residual stress distribution in the A992 W12×87 and A913 Grade 80 W14×808 sections was predicted accurately despite excluding the k-zone geometry.

Furthermore, the flexural buckling strength of the W12×87 section matched well with reference results supporting the validity of the modeling assumptions for global buckling behavior. While this simplification is justified for the scope of this study—focused on global flexural buckling response—it is indeed possible that inclusion of the k-zone could be important in future studies concerned with local instability, stress concentration effects, or failure initiation at the flange-web interface.

FLEXURAL BUCKLING CURVES FOR A992 STEEL COLUMNS

Initially, column flexural buckling curves are developed based on the simulation for selected W-shapes using A992 steel to recreate the past work on mild steel and characterize the expected uncertainty between known column behavior and the current AISC 360-22 column curve. The W-shapes chosen for the analysis are presented in Table 2 with their corresponding height-to-width ratio, h/b, flange thickness, t_f, width-to-thickness, $b_f/2t_f$, and web slenderness, h/t_w, ratios. The shapes are chosen for a wide range

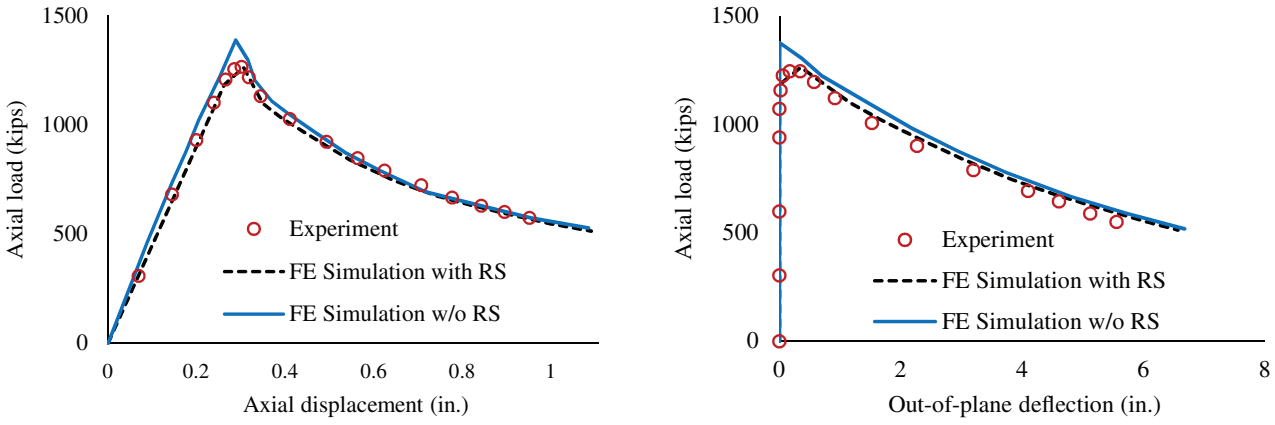

(a) Axial load displacement *(b) Axial load-lateral deflection*

Fig. 13. Buckling analysis vs. experimental (data from Lamarche and Tremblay, 2011) responses under monotonic axial loading for ASTM A992 W12×87 section.

of these ratios so that the analyses can capture their effect on the flexural buckling resistance of the columns. The columns are analyzed up to a slenderness ratio, KL/r, of 200. Finite element analyses are performed on these shapes by changing the slenderness ratio of the column using different column lengths, and the buckling strengths are determined for different slenderness ratios about both minor and major axes using A992 steel with a yield stress of 50 ksi. Because the column is considered pin-connected at both ends, the effective length factor K is taken as 1.0. To make the column curves comparable between different W-shapes having different radii of gyrations about the minor and major axes, and different yield strengths of steel, the critical buckling strength, F_{cr} is normalized by the yield stress, F_y, which is the same as the reduction factor χ in Eurocode 3, and it is plotted against the relative slenderness ratio λ as given by Equation 1. Note that the initial geometric imperfection is taken as $L/1500$ at the mid-height of the column to be comparable with the AISC 360 column curve, and for each of the shape, the simulated residual stresses are considered as the initial state of stress. Figure 14 shows column buckling curves about minor and major axes for six sections of Table 2 made of A992 steel along with their design curves as given by AISC 360 (2022) and Eurocode 3 (CEN, 2005a).

From these figures, it is observed that the simulated column flexural buckling curves for the sections presented in Table 2 about the major axis are close to the AISC 360 and EC3 column design curves. The simulated flexural buckling resistances are on the AISC 360 column curve for small ($\lambda < 0.5$) and large ($\lambda > 1.5$) slenderness ratios, indicating that for the local and elastic buckling range, the AISC 360 column buckling curve agrees well with the simulated responses. For inelastic buckling range with intermediate slenderness ratios ($0.5 \le \lambda \le 1.5$), both the AISC 360 and Eurocode 3 column design curves underestimate the simulated major axis buckling strengths of A992 sections. However, the degree of underestimation is more pronounced for Eurocode 3, which predicts lower strengths across the full slenderness range compared to AISC. For the sections studied, AISC 360 underestimates the simulated strength by approximately 5–10%, while EC3 underestimates by a larger margin, particularly in the intermediate slenderness range ($0.5 \le \lambda \le 1.5$).

Similar to major axis buckling, simulated minor axis buckling curves as shown in Figures 14 and 15 for the sections in Table 2 agree well with the AISC 360 and EC3 column design curves for small ($\lambda < 0.5$) and large ($\lambda > 1.5$) slenderness ratios, indicating that for the local and elastic buckling range, AISC 360 and EC3 column buckling curves agree well with the simulated responses. However, in the inelastic buckling range with intermediate slenderness ratio ($0.5 \le \lambda \le 1.5$), the AISC 360 column curve agrees well with the simulated column curve for nonheavy sections with $t_f \le 1.5$ in. with $b_f/2t_f \ge 5.45$, and $h/t_w \ge 12.8$ (e.g., W14×53, W14×82, W12×87, W14×145, and W14×193) and overestimates the buckling capacity for heavy sections with $t_f >$ 1.5 in. with $b_f/2t_f < 5.45$, and $h/t_w < 12.8$ (e.g., W14×257, W14×426, W12×336, W14×605, and W14×808). The residual stress distribution pattern in all these sections is more or less similar, with tensile residual stresses at the center of the flange and compressive residual stresses at the edges of the flange [see Figures 8(a) and 10(a)], and compressive residual stress in the middle of the web and tensile residual stresses the ends of the web [see Figures 8(b) and 10(b)]. Since inelastic flexural buckling of columns is preceded by flange local buckling, the magnitude and distribution of the compressive residual stress in the flange plays a substantial role in the flexural buckling strength of the columns. For lighter W-shape sections, the maximum compressive residual stress in the flange is relatively small compared to the higher residual stresses typically developed in heavier sections. For example, in the W14×82 column section, the maximum compressive stress on the flange is ~8.6 ksi [Figure 16(a)], whereas for a W14×426, the maximum compressive stress on the flange is ~23.3 ksi [Figure 16(b)].

Moreover, the maximum compressive stress develops at the center of the web for a W14×82 section, whereas the compressive stress is maximum at the edge of the flange and at the center of the web for a W14×426 section. As a result of high compressive residual stresses on the flange, the heavier shapes develop local instability earlier than the nonheavy shapes followed by global instability. The AISC 360 column curves were developed based on the Galambos and Ketter (1959) residual stress model considering a linear distribution of residual stresses with a magnitude of $0.3F_y$ tensile at the center of the flange and $-0.3F_y$ compressive at the edges of the flange and uniformly distributed tensile residual stress throughout the depth of the web. The simulated compressive residual stresses on the flange of heavy shapes are substantially higher than those considered in the Galambos and Ketter (1959) model. Additionally, both tensile and compressive residual stresses are observed on the web of the section from the simulation, which is not considered in the Galambos and Ketter (1959) model. As a result, the flexural buckling strengths of the heavier columns are less than the AISC 360 column curve for $0.5 \le \lambda \le 1.5$, which is typically the inelastic buckling range. For example, within the relative slenderness range between 0.5 and 1.5, the AISC 360 column curve overestimates the column buckling capacity of A992 steel columns by 12% for the W14×426 section. This is consistent with the findings of ECCS Technical Committee 8 (2008), where they confirmed that residual stresses in larger hot-rolled sections increase disproportionately due to slower cooling rates, lowering their buckling resistance. As noted from Figure 1, EC3 column buckling curves are overly conservative for all the sections in the intermediate slenderness ratios. Eurocode 3 Part 1-1 (CEN, 2005a), considers these

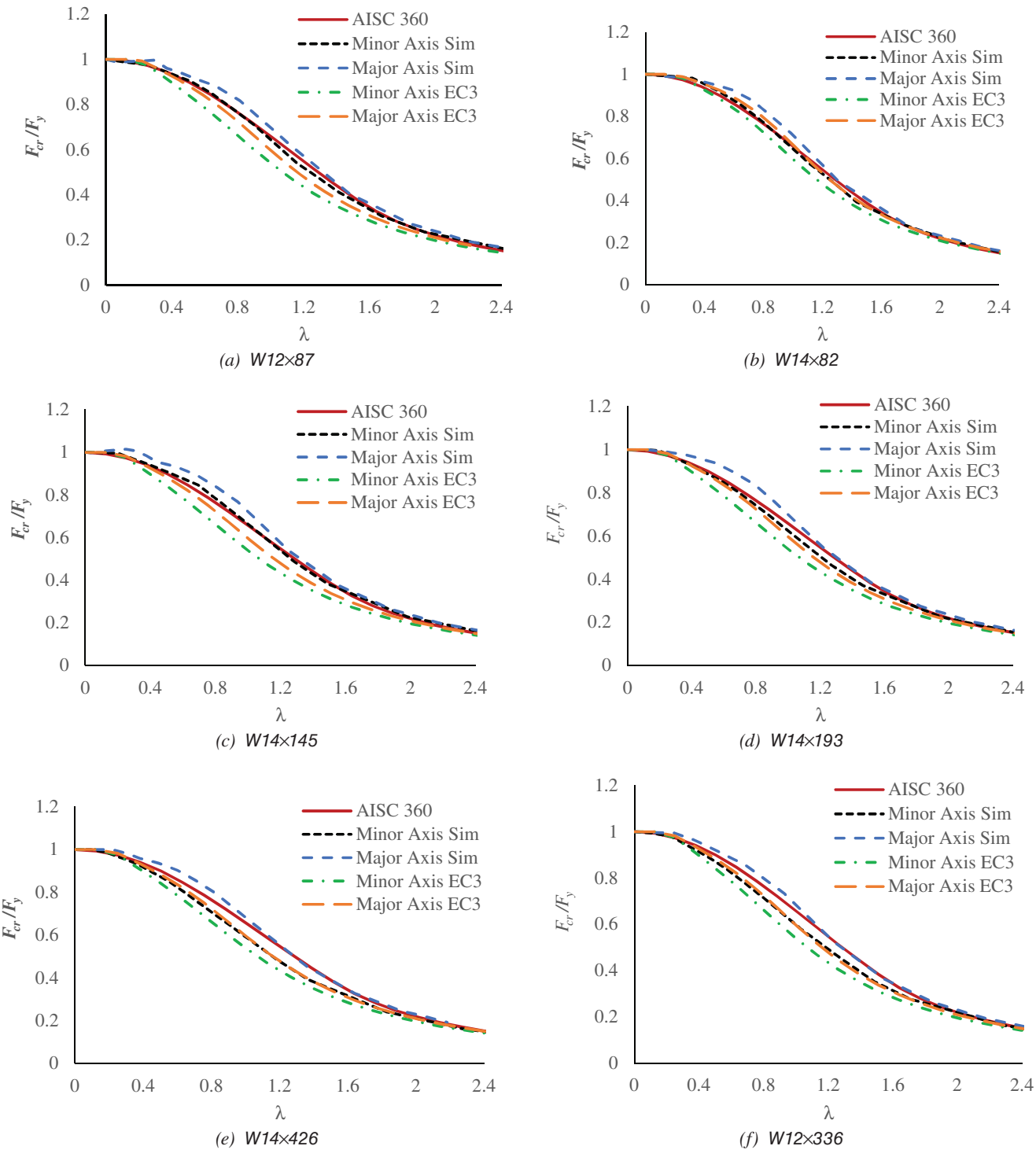

(a) W12×87 (b) W14×82

(c) W14×145 (d) W14×193

(e) W14×426 (f) W12×336

Fig. 14. Column flexural buckling curves for A992 steel sections.

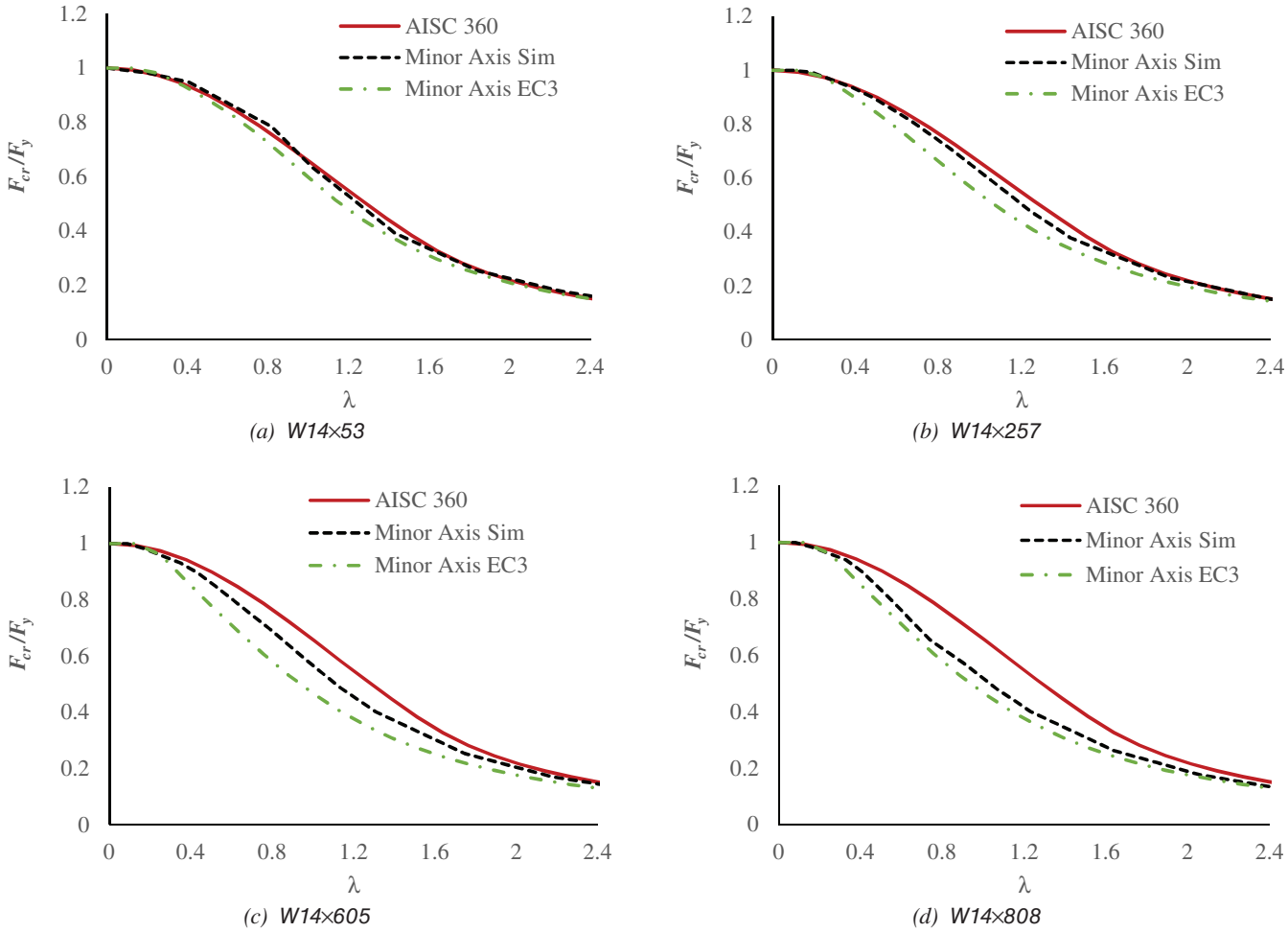

(a) W14×53 (b) W14×257

(c) W14×605 (d) W14×808

Fig. 15. Column flexural buckling curves about the minor axis for A992 steel sections.

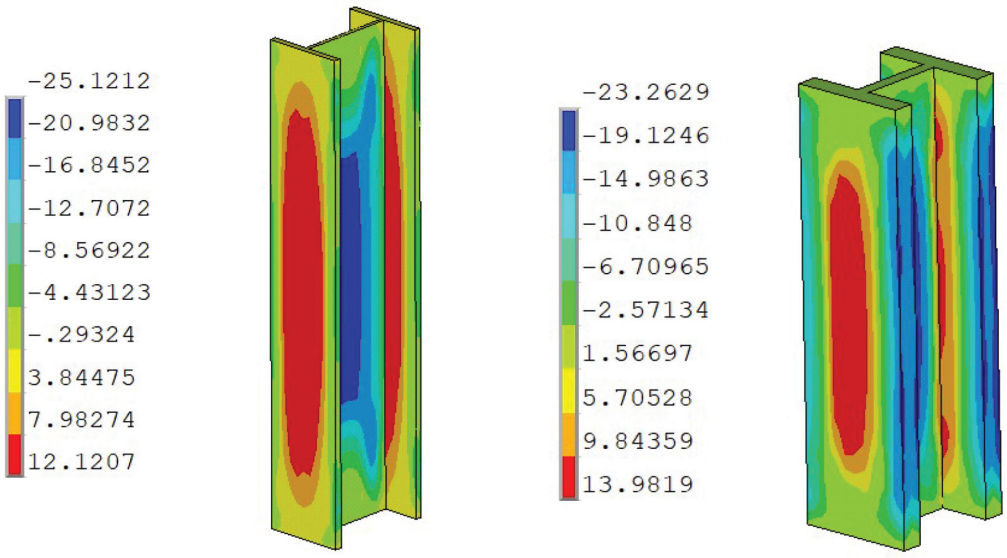

(a) W14×82 (b) W14×426

Fig. 16. Simulated longitudinal residual stress contour (in ksi) of A992 steel sections.

Table 3. Cross-Sectional Properties of W-Shapes Investigated for F_y = 80 ksi Steel Column Buckling Curves				
Column Designation	h/b	t_f (in.)	$b_f/2t_f$	h/t_w
W14×808	1.23	5.12	1.82	3.04
W14×605	1.20	4.16	2.09	4.39
W14×500	1.15	3.50	2.43	5.21
W14×426	1.12	3.04	2.75	6.08
W14×342	1.07	2.47	3.31	7.41
W14×257	1.03	1.89	4.23	9.71
W14×211	1.00	1.56	5.06	11.6
W14×193	0.99	1.44	5.45	12.8
W14×176	0.97	1.31	5.97	13.7
W14×145	0.96	1.09	7.11	16.8
W14×132	1.00	1.03	7.15	17.7
W14×120	0.99	0.94	7.80	19.3
W14×90	0.97	0.71	10.2	25.9
W14×82	1.41	0.855	5.92	22.4
W14×68	1.40	0.72	6.97	27.5
W14×53	1.94	0.66	6.11	30.9
W12×87	1.03	0.81	7.48	18.9
W12×336	1.25	2.96	2.26	5.47

variations in the residual stresses and geometric imperfections based on the geometry of the shapes by incorporating the imperfection factor. EC3's five different buckling curves, a_0, a, b, c, and d depend on the section's h/b ratio and flange thickness, t_f. As per EC3, the W14×426 section belongs to column curve b with an imperfection factor of 0.34. The corresponding column curve developed based on the EC3 is plotted in Figure 14(e) for section W14×426, where it is observed that the EC3 column curve accounted for this reduction in the buckling strength in the inelastic buckling range; however, the EC3 curves are overly conservative compared to the simulated responses and AISC 360 column curves. Based on the responses using A992 steel, it is demonstrated that the finite element models developed in this study provide reliable column buckling capacity prediction for rolled shapes; hence, the models are further utilized to investigate the column buckling capacity of rolled shapes using A913/A913M Gr. 80 steel.

FLEXURAL BUCKLING CURVES FOR A913/A913M GRADE 80 STEEL COLUMNS

In this section, comparisons are made between the simulated column buckling curves using A913/A913M Gr. 80 steel and AISC 360 (2022b) and EC3 (CEN, 2005a) column design curves to understand how effectively the AISC 360 column design curve predicts the flexural buckling capacity of high-strength steel rolled shape columns. Finite element analyses are performed on 17 W14 and 2 W12 sections as shown in Table 3, using the validated finite element model with multilinear kinematic hardening material model and $L/1500$ bow imperfection. Residual stresses are incorporated by using the sequentially coupled thermo-mechanical analysis as discussed in the "*Modeling of Residual Stresses*" section for all the shapes using A913/A913M Gr. 80 steel. The residual stress distribution for six of the shapes of Table 3 using A913/A913M Gr. 80 steel are presented in Figure 17. While all listed W-shape sections were modeled using A913 Grade 80 material properties, not all are currently produced in accordance with ASTM A913 due to QST process limitations, which require a minimum flange and web thickness to achieve proper self-tempering. In particular, lighter sections such as W14×82, W14×68, W14×53, and W12×87 may not meet this requirement and are not typically available from producers offering A913 Grade 80. These shapes were included in the numerical study for comparative and parametric analysis purposes only to explore the sensitivity of flexural buckling strength across a broader geometric spectrum.

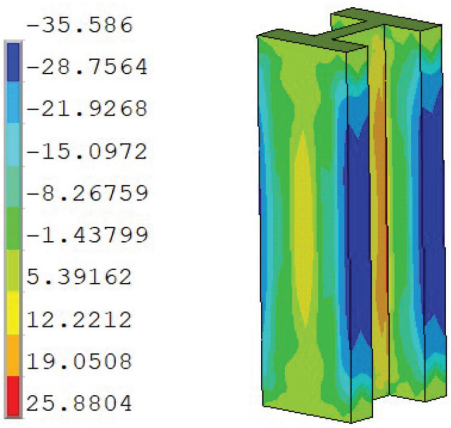

(a) W14×808

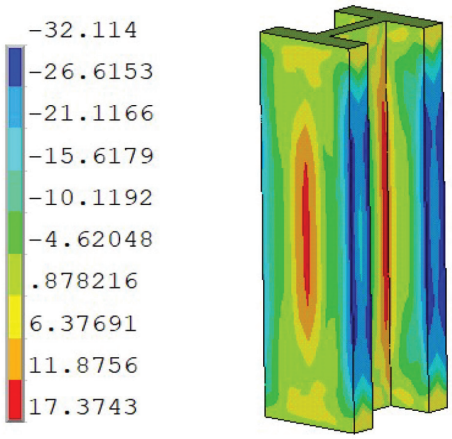

(b) W14×605

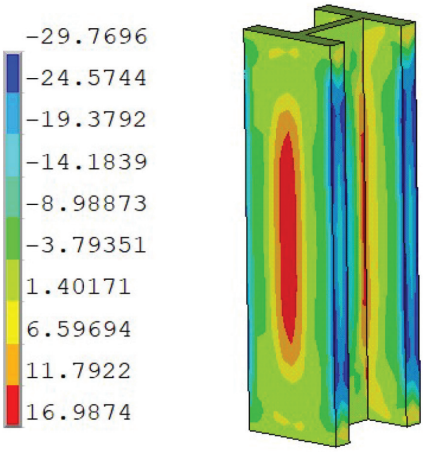

(c) W14×426

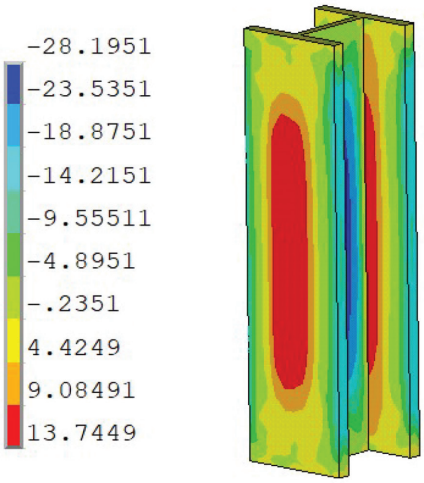

(d) W14×257

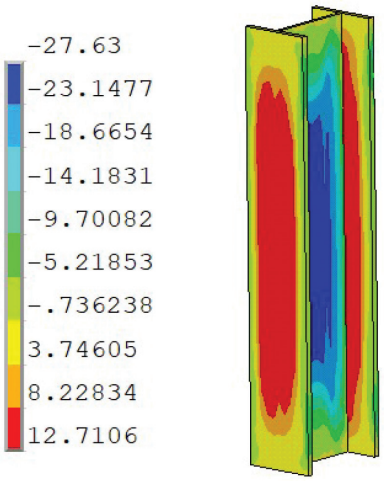

(e) W14×82

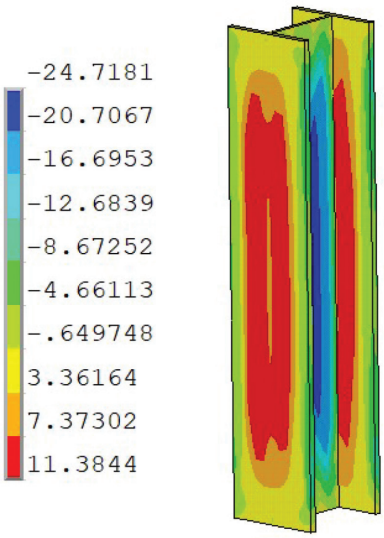

(f) W12×87

Fig. 17. Simulated longitudinal residual stress contour (in ksi) of A913 Gr. 80 steel sections.

Note that European research has suggested that high-strength steels, such as S460 (yield stress of 460 MPa or 65 ksi), have different residual stress distributions, strain-hardening behavior, and imperfections sensitivity compared to lower-grade steels. As a result, Eurocode 3 proposed separate curves for high-strength steel S460 based on the cross-section type (I-section, box, circular, etc.), the buckling mode (minor/major axis), and the fabrication method (rolled vs. welded). In addition, study by Snijder et al. (2014) demonstrated that the EC3 buckling curves for S460 high-strength steel columns can also be used to predict the buckling strength of S500 (yield stress of 72 ksi) high-strength steel columns. Figures 18, 19, and 20 present comparisons of the simulated column buckling curves with the AISC 360 and EC3 design column curves for the sections shown in Table 3 for buckling about both the minor and major axes.

Based on the observations of the simulated column buckling curves using A913/A913M Gr. 80 steel, it is noted that the simulated column curves show differences from the AISC 360 and EC3 column design curves within the relative slenderness values of 0.3–1.5 for buckling about the minor axis and within relative slenderness values 0.5–2 for buckling about the major axis, which is typically the inelastic buckling range for the columns. For smaller and larger relative slenderness ratios, the simulated column curves agree well with the AISC 360 and EC3 column curves, which are typically the compression yielding and elastic buckling range of the columns. From the simulated column curves, it is observed that both the AISC 360 and EC3 column design curves underestimate the major axis buckling capacity for all the sections analyzed. The percent increase in the simulated buckling strength compared to the AISC 360 column design curve varies between 3 and 14% depending on the λ values, h/b ratio, and the flange thickness of the sections as shown in Figures 21, 22, and 23.

Sections with $h/b \geq 1.12$ and flange thickness t_f more than 3 in. such as W14×808, W14×605, W14×500, and W14×426 sections show less of an increase in the buckling capacity, whereas sections with $h/b < 1.12$ and flange thickness t_f less than 3 in. such as W14×193, W14×145, W14×120, and W14×90 demonstrate a substantial increase in the buckling capacity compared to the AISC 360 column design curve. For example, at $\lambda = 0.5$, 0.75, and 1, the percent increase in the simulated major axis buckling capacity vary between 3 and 8% for sections with flange thickness more than 3 in., as shown in Figures 21–23. On the other hand, the percent increase in the simulated major axis buckling capacity vary between 8 and 14% for sections with flange thickness less than 3 in. at $\lambda = 0.5$, 0.75, and 1.0. For sections W14×53, W14×68, and W14×82, the simulated column buckling curves do not show a significant increase in the buckling capacity, even though the flange thickness is less than 1 in.

These sections have a higher h/b ratio, which is in the range of 1.4–1.94. The simulated column buckling curves about the minor axis are compared with the AISC 360 and EC3 column curves in Figures 18–20. It is observed that for heavy sections with $h/b \geq 1.12$ and $t_f \geq 3$ in. such as W14×808, W14×605, W14×500, and W14×426, the AISC 360 column curve overestimates the buckling capacity that depends on the λ values, h/b ratio, and the flange thickness of the sections. This is mostly observed in the inelastic buckling range with λ values between 0.4 and 1.5. These heavy shapes develop high compressive residual stresses in the flanges, and as a result, the thicker the flange, the higher the overestimation for heavy sections with $h/b \geq 1.12$ and $t_f \geq 3$ in. Nevertheless, the overestimation is in the range of 2–8% depending on the h/b ratio and the flange thickness of the sections as shown in Figures 21–23. For sections with $h/b < 1.12$ and $t_f < 3$ in, the AISC 360 column design curve underestimates the buckling strength of A913/A913M Gr. 80 columns between λ values of 0.3 and 1.5, and it is observed that as the h/b value and the flange thickness decrease, the difference between the simulated column buckling strength about the minor axis and the AISC 360 column design curve increases. It is noted from Figures 21–23 that the AISC 360 column curve underestimates the buckling capacity about minor axis by 4–11%, depending on the flange thickness and h/b ratio of the section for λ values between 0.3 and1.5.

For sections with $1.00 \leq h/b \leq 1.12$ and $1.56 \leq t_f \leq 3.00$ in., the simulated column buckling curves about the minor axis exhibit a 5% increase compared to the AISC 360 column curve, whereas for any sections with $h/b < 1.00$ and $t_f < 1.56$ in., the simulated column buckling curves about the minor axis are 5–11% stronger than the AISC 360 column curve. For sections W14×53, W14×68, and W14×82, the simulated column buckling curves do not show substantial increase in the buckling capacity even though the flange thickness is less than 1 in. These sections have a higher h/b ratio, which is in the range of 1.4~1.94. On the contrary, for λ values between 0.4 and 1.5, EC3 column buckling curves underestimate the buckling capacity for heavy sections with $h/b \geq 1.2$ and $t_f \geq 4$ in., such as for W14×873, W14×808, and W14×605 sections, even though EC3 has separate curves for 65 ksi high-strength steel. However, for sections with $h/b < 1.2$ and $t_f < 4$ in., the simulated column buckling curves about the minor axis agree well with the EC3 S460 high-strength column curves in the inelastic buckling range. For elastic buckling range and compression yielding, the simulated column buckling curves about the minor axis agree well with both the AISC 360 and EC3 column curves. Moreover, note that the major axis buckling curves for all the sections analyzed are always higher than the minor axis buckling curves. This indicates that using the same design curve for major and minor axis buckling may underestimate

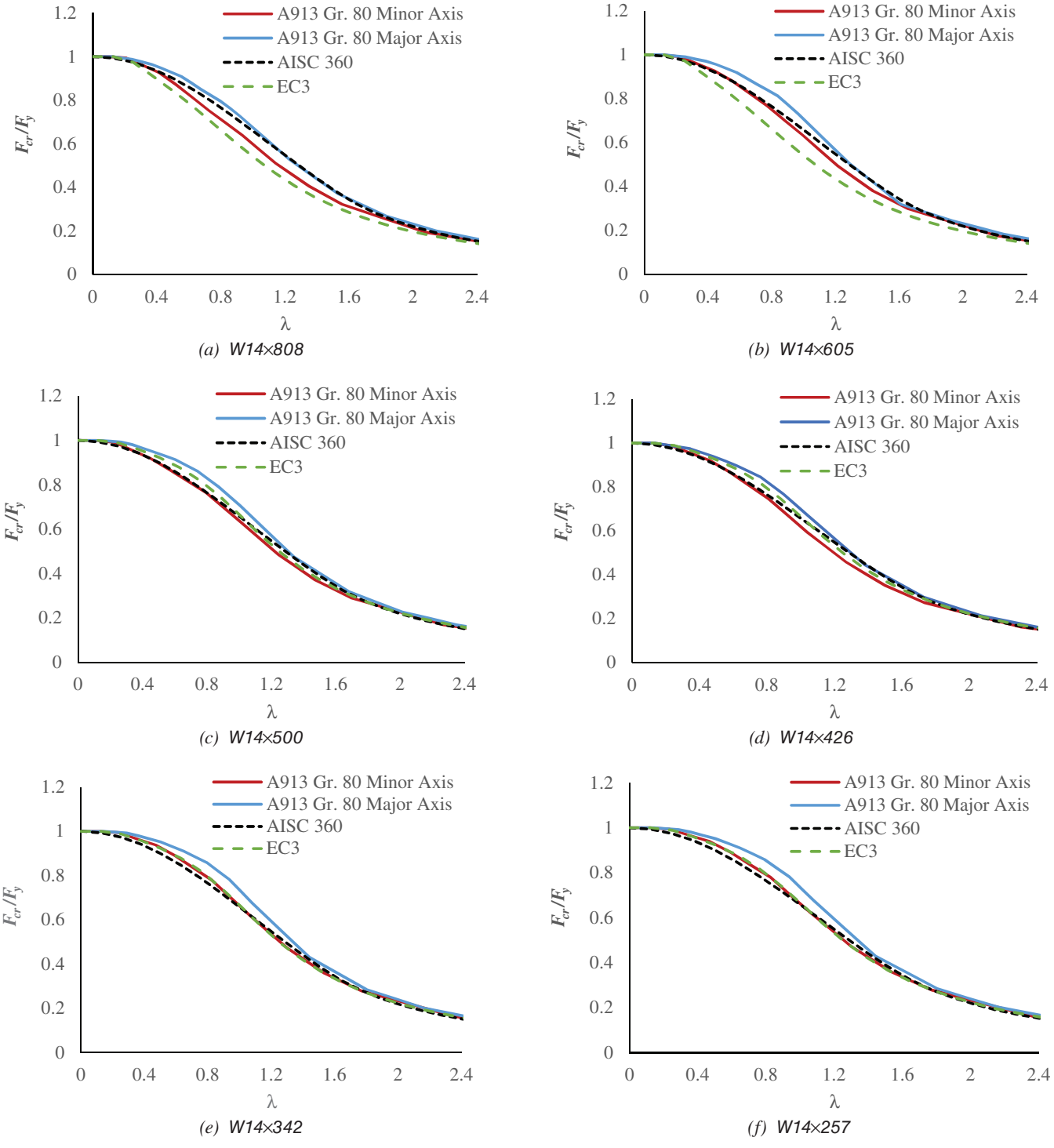

(a) W14×808 *(b) W14×605*

(c) W14×500 *(d) W14×426*

(e) W14×342 *(f) W14×257*

Fig. 18. Column flexural buckling curves for A913/A913M Gr. 80 steel sections.

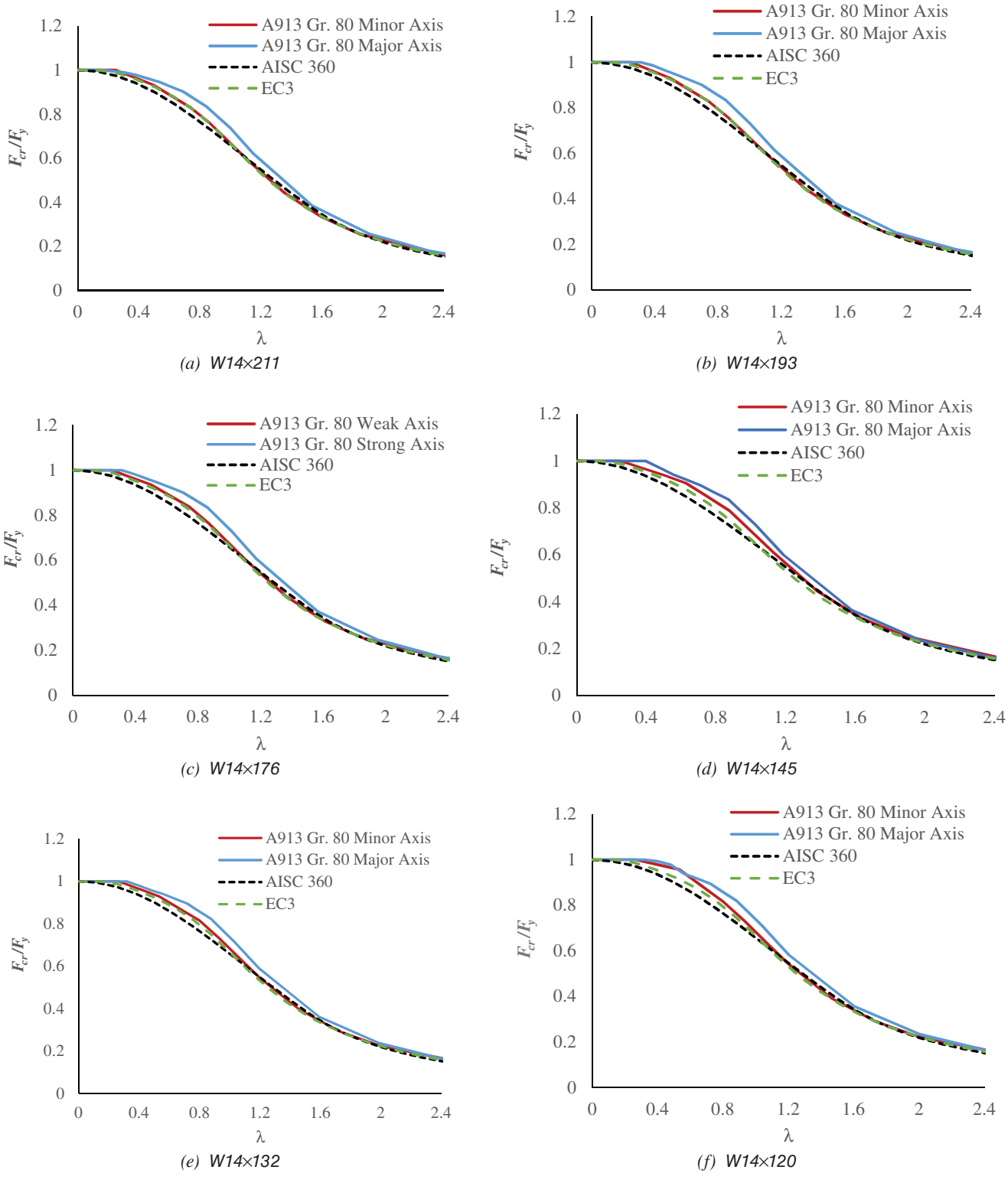

(a) W14×211 (b) W14×193

(c) W14×176 (d) W14×145

(e) W14×132 (f) W14×120

Fig. 19. Column flexural buckling curves for A913/A913M Gr. 80 steel sections.

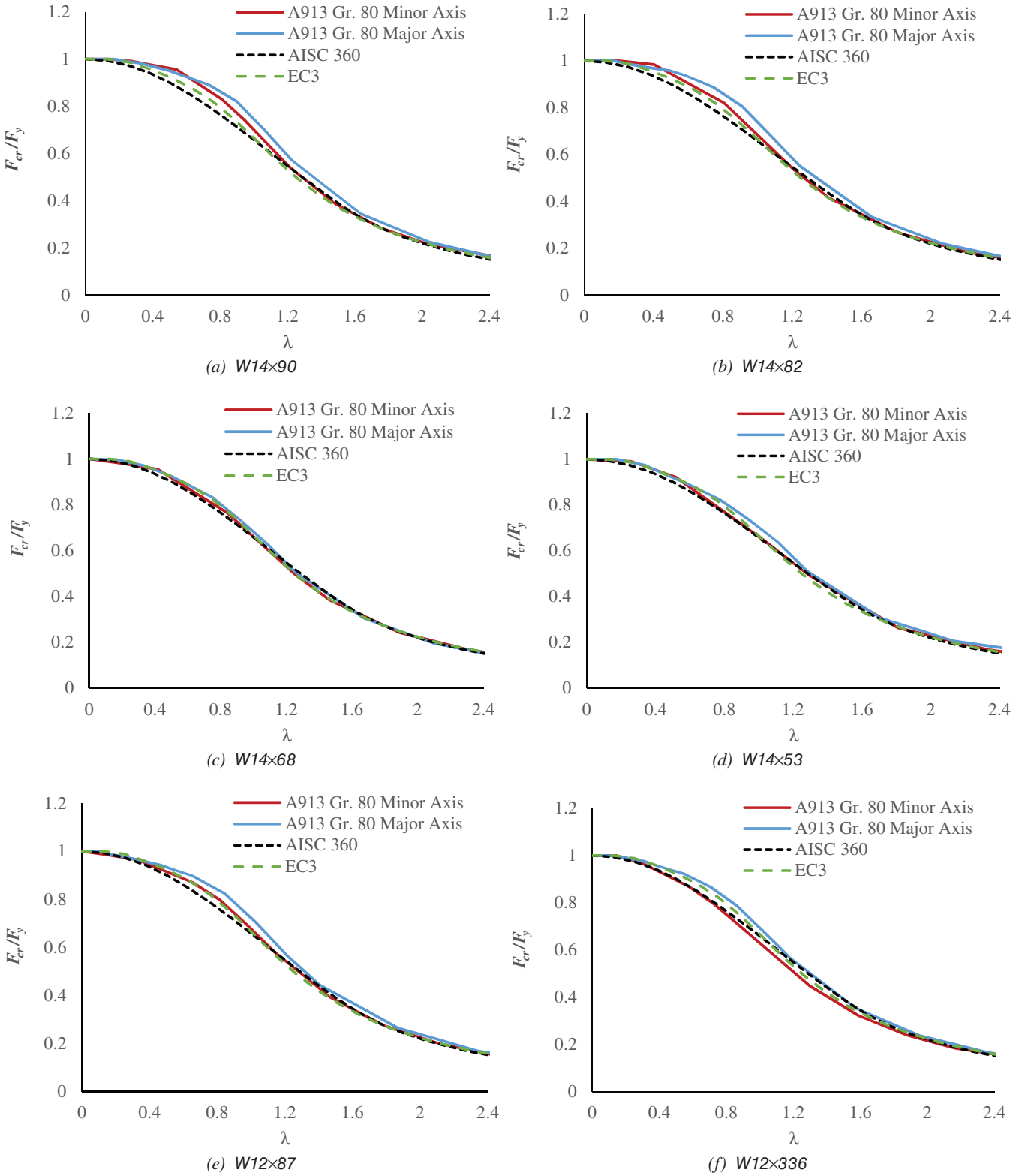

Fig. 20. Column flexural buckling curves for A913/A913M Gr. 80 steel sections.

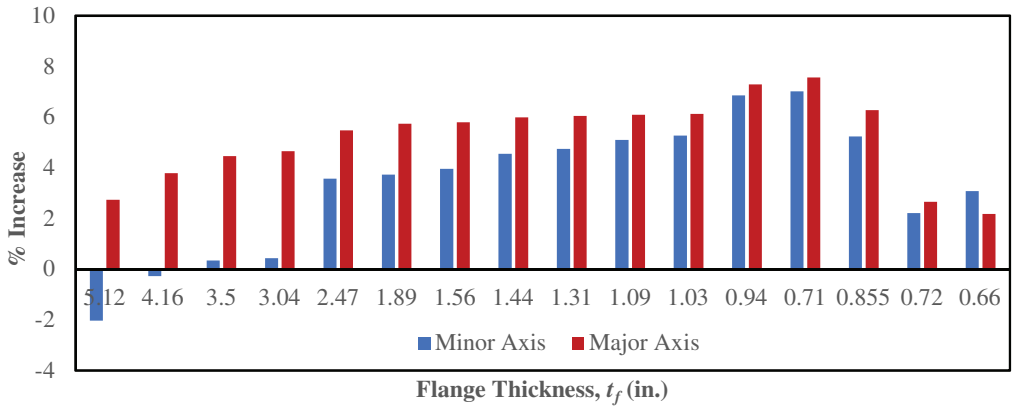

Fig. 21. Percent difference between the simulated and AISC 360 column buckling curves of ASTM A913 Gr. 80 W-shape sections for different flange thickness for λ = 0.5.

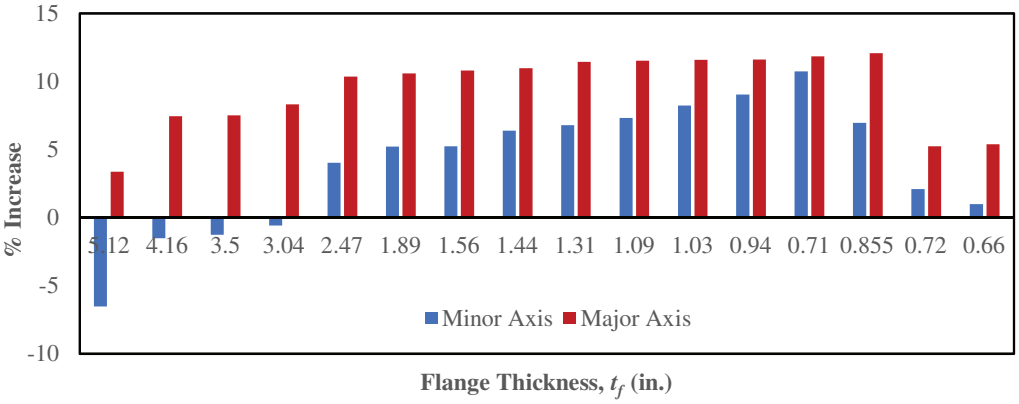

Fig. 22. Percent difference between the simulated and AISC 360 column buckling curves of ASTM A913 Gr. 80 W-shape sections for different flange thickness for λ = 0.75.

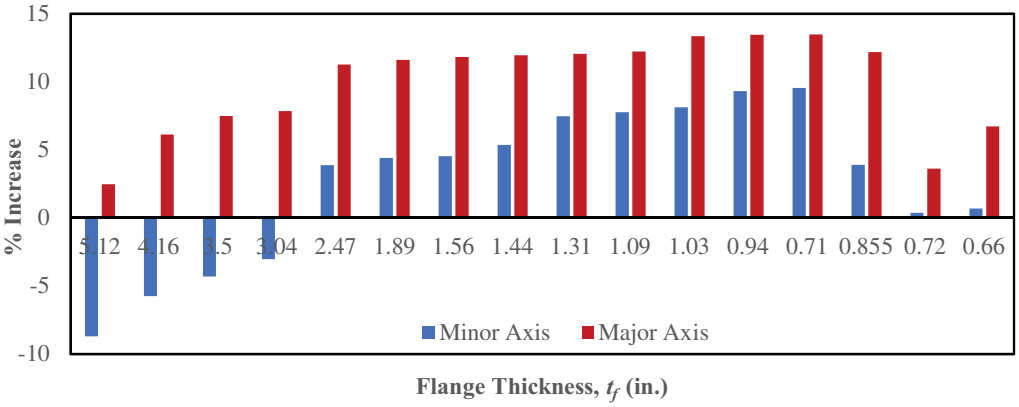

Fig. 23. Percent difference between the simulated and AISC 360 column buckling curves of ASTM A913 Gr. 80 W-shape sections for different flange thickness for λ = 1.0.

the buckling strength of the columns about the major axis significantly, especially for high-strength steels.

This was accounted for in the development of column design curves for stainless steel in AISC 370 (2021), where separate buckling curves for minor and major axis are proposed. In summary, A913/A913M Gr. 80 steel columns exhibit higher flexural buckling strength about both minor and major axes for intermediate slenderness values compared to the AISC 360 column curves. This increase in the flexural buckling strength is applicable for sections with $h/b < 1.2$ and $t_f < 3$ in. and can range from 5–11% for minor axis buckling and 5–14% for major axis buckling. For heavy shapes, the AISC 360 column curve overpredicts the flexural buckling capacity by 2–8% due to the presence of high compressive residual stresses on the flanges as discussed in the "Modeling of Residual Stresses" section. These results suggest that while the AISC 360 column design curve performs reasonably well for many cases, its direct application to high-strength steel columns such as A913/A913M Gr. 80 may lead to unconservative or overly conservative predictions depending on the section geometry. Therefore, potential modifications or refinements to the current design curve may be warranted to improve accuracy for high-strength applications.

A913/A913M GRADE 80 VS. A992 COLUMN FLEXURAL BUCKLING CURVES

Now let's compare the simulated column buckling curves of the A913/A913M Gr. 80 steel columns with those of the columns made of A992 steel and also, how they compare with the AISC 360 column design curve. Figure 24 presents a comparison of A992 and A913/A913M Gr. 80 steel column buckling curves about both the minor and major axes with the AISC 360 column curve for several sections with different h/b ratios and flange thicknesses, namely, W14×426, W12×336, W14×193, W14×145, W12×87, and W14×82. It is observed that for $\lambda = 0.5$~2, the major axis buckling curves for A992 steel columns are 3–12% stronger than the AISC 360 column curves, whereas the major axis buckling curves for A913/A913M Gr. 80 steel columns are 5–14% stronger than the AISC 360 column curves. The column buckling curves for A913/A913M Gr. 80 steel columns about the major axis is always 2–5% stronger than those of the A992 steel columns, regardless of the sectional dimensions and λ values between 0.5~2.0. On the contrary, the simulated buckling curves about the minor axis for A913/A913M Gr. 80 steel columns are always stronger than the relevant column buckling curves for A992 steel columns between $\lambda = 0.3$~1.5. For example, the minor axis buckling curves for W14×82 and W14×145 sections where the thickness of the flange is less than 1.56 in., AISC 360 column design curve underestimates the buckling strength of A913/A913M Gr. 80 columns by 5–11% between λ values of 0.3 and 1.5, whereas, the buckling strength of A992 columns are predicted correctly by the AISC 360 column curve [see Figures 24(d) and 24(f)]; that is—the column buckling curves for A913/A913M Gr. 80 steel columns are 5–11% stronger than the column curves for A992 steel columns.

As the flange thickness increases to 2.96~3.04 in. for W12×336 and W14×426 sections, the simulated column curves about the minor axis for A913/A913M Gr. 80 steel columns are 8–10% stronger than the corresponding column curve for A992 steel column between λ values of 0.5 and 1.5 [see Figures 24(a) and 24(b)]. When the thickness of the flange is further increased to around 4.16 and 5.12 in. for W14×605 and W14×808 sections, respectively, AISC 360 column design curve overestimates the buckling strength compared to both A913/A913M Gr. 80 and A992 steel columns; however, the buckling strengths of A913/A913M Gr. 80 steel columns are still 8–16% stronger than the corresponding column buckling strengths of A992 steel columns in the inelastic buckling range [see Figures 25(a) and 25(b)]. On average, for the sections considered in this study, the buckling strength of A913/A913M Gr. 80 steel columns about the minor axis is around 8–12% higher than that of A992 steel columns, and it depends on the h/b ratio and the flange thickness of the sections, which is consistent with the Eurocode 3, Part 1-1 (CEN, 2005a). In addition, Eurocode 3, Part 1-1, dictated that high-strength steel columns exhibit higher flexural buckling strengths than conventional grade steel columns regardless of the sectional dimensions, which is consistent with the findings of this study where it is observed that A913/A913M Gr. 80 steel column possesses 8–12% higher buckling strength about the minor axis and 2–5% higher buckling strength about the major axis than the corresponding A992 steel column in the inelastic buckling range for the sections considered in this study.

CONCLUSIONS

This study investigated the flexural buckling behavior of wide-flange rolled steel columns fabricated from both conventional structural steel (ASTM A992, $F_y = 50$ ksi) and high-strength steel (ASTM A913 Grade 80, $F_y = 80$ ksi). A suite of nonlinear finite element simulations was conducted incorporating measured material stress-strain behavior, realistic geometric imperfections, and residual

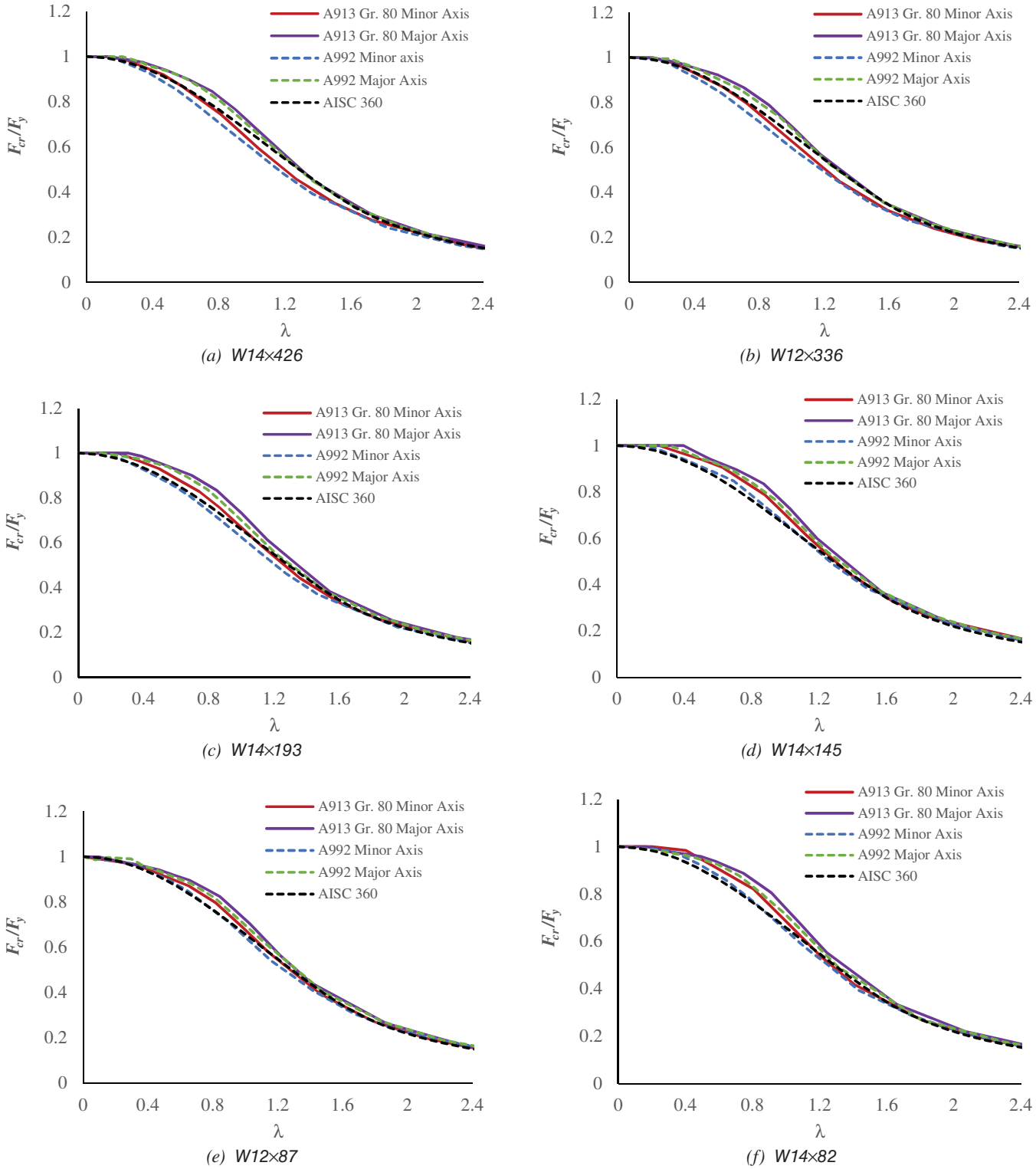

Fig. 24. Simulated column flexural buckling curves for sections using A913/913M Gr. 80 and A992 steels.

stress distributions obtained through sequentially coupled thermomechanical analysis. Simulated buckling responses were used to generate column curves over a broad range of slenderness ratios and section geometries, enabling direct comparison with the AISC 360-22 and Eurocode 3 (EC3) design curves.

Results for A992 columns show that the AISC 360-22 unified column curve generally captures flexural buckling strength with reasonable accuracy in major axis buckling, with underpredictions of 5–10% in the intermediate slenderness range ($\lambda = 0.5$~2.0). However, for minor axis buckling of nonheavy sections with $h/b \leq 1.0$ and $t_f \leq 1.5$ in., the AISC 360-22 column buckling curve agrees well with the simulated responses; however, for minor axis buckling of heavy sections with $h/b > 1.0$, $t_f > 1.5$ in., AISC 360 overestimates capacity by 10–15% in the inelastic buckling range due to elevated compressive residual stresses on the flanges. In contrast, EC3 column curves were uniformly more conservative, particularly in the inelastic range. These findings suggest that for heavier W-shapes, particularly in minor axis buckling, some modification to the AISC 360-22 design curve may be worthy of consideration to improve accuracy and prevent overestimation of capacity.

For A913 Gr. 80 columns, the AISC 360 curve remained acceptable overall, yet underpredictions of 5–12% about the minor axis and 5–14% about the major axis were observed depending on slenderness and section classification. In nonheavy sections ($h/b < 1.12$, $t_f < 3$ in.), the AISC 360 curve underpredicted buckling strength in the inelastic buckling range, while for heavier sections, it overpredicted capacity. Additionally, the flexural buckling strengths of A913 columns in the inelastic buckling range were consistently 5–12% higher than those of A992 counterparts, especially in the minor axis direction. These trends indicate that the current AISC 360 curve performs acceptably for $F_y = 80$ ksi steel; nevertheless, it highlights a potential for material and section-specific adjustments to the AISC 360 design curve in the inelastic buckling range when applied to high-strength rolled shapes and heavier sections. However, the moderate gains from developing a new curve specific to this grade may not justify the complexity, especially considering the results for $F_y = 50$ ksi already show a mix of under- and overpredictions. In that context, proposals for a new design curve for $F_y = 80$ ksi should carefully weigh the benefits of localized conservatism reduction against the risks of unconservative predictions in other regimes.

While the findings affirm the general applicability of the AISC 360-22 unified curve to both A992 and A913 rolled shapes, they also reveal nuances in performance that depend on cross-sectional proportions, loading direction, and residual stress profiles. A single unified curve may not fully capture these effects, particularly for heavy or high-strength shapes with $F_y \geq 80$ ksi buckling in the inelastic range. Although this study does not propose a new column curve, it highlights the potential limitations of the existing design provisions and lays the groundwork for further research. As such, future research should explore the viability of shape-dependent or strength-tiered column curves. Full-scale experimental validation will be essential to confirm these numerical trends and guide refinement of design provisions. Collaboration between academic researchers and industry partners—including ongoing discussions within the AISC technical committees—will be vital to advancing the adoption of high-strength steel in design practice and improve the safety-efficiency balance in modern high-strength steel design.

Ultimately, this study underscores that while the current design provisions are generally effective, their limitations should be acknowledged, especially when applied to rolled shapes fabricated from emerging high-strength steels.

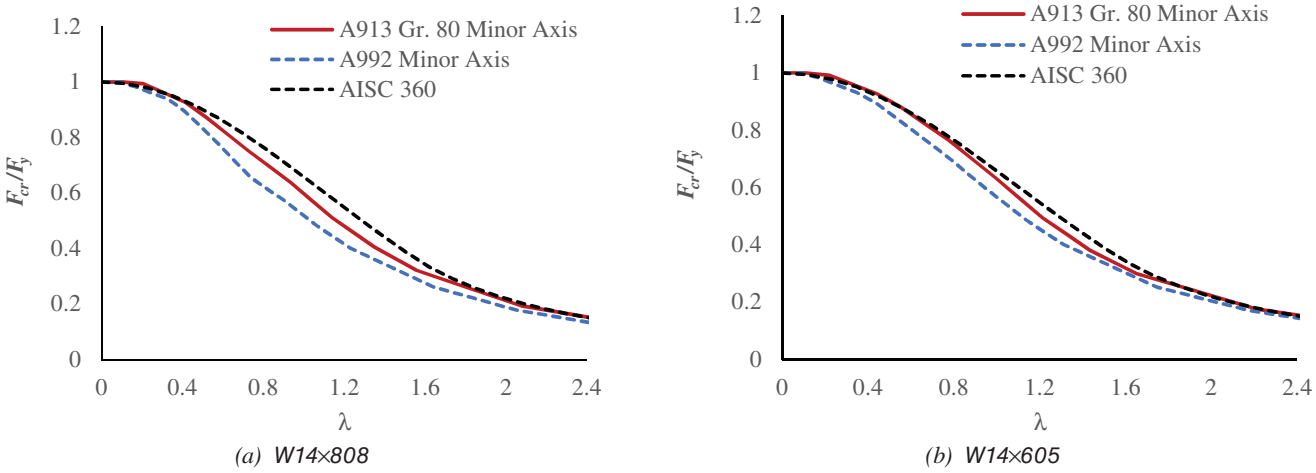

(a) W14×808 (b) W14×605

Fig. 25. Simulated column buckling curves about the minor axis for sections using A913/913A Gr. 80 and A992 steels.

Refinement—not replacement—of existing curves, with attention to shape, strength level, and directional sensitivity, appears to be a more realistic and impactful approach.

FUTURE TASKS

Future work may explore the development of column buckling curves for high-strength hollow structural sections (HSS), which differ substantially from rolled W-shapes in both manufacturing process and residual stress behavior. Unlike ASTM A913, which applies to hot-rolled W-shapes, high-strength HSS products are typically fabricated from cold-formed and welded plate or strip materials governed by ASTM A500 (2021a) or ASTM A1085 (2015) specifications. These differences affect geometric tolerances, residual stress distributions, and imperfection sensitivity. Accordingly, any extension of buckling curve calibration to high-strength HSS will require a tailored modeling approach that reflects these characteristics and production constraints.

While this study does not propose a new design equation, the validated numerical framework and consistent trends observed—particularly the underestimation of strength for A913 Gr. 80 rolled sections—form the basis for future reliability-based calibration. Future work will expand the simulation database to include additional W-shapes and HSS sections and will evaluate whether separate or modified buckling curves are warranted for A913 Gr. 80 or higher strength steels. The methodology will follow reliability provisions in AISC 360, Appendix 1, and incorporate statistical variability in material properties and geometric imperfections.

ACKNOWLEDGMENTS

The author is grateful to AISC for funding this research and for sharing all the relevant information for this project. However, any opinions presented in this paper are solely those of the author. The author also greatly acknowledges the A913 Gr. 80 high-strength steel material testing data provided by steel producers and coordinated through AISC. The guidance provided by Professor Ronald Ziemian from Bucknell University, Professor Benjamin Schafer from Johns Hopkins University, and Dr. Devin Huber from AISC throughout the completion of this project is greatly appreciated.

REFERENCES

AISC (2016), *Specification for Structural Steel Buildings*, ANSI/AISC 360-16, American Institute of Steel Construction, Chicago, Ill.

AISC (2019), "High Strength Steel," Task Group Report prepared by the AISC Committee on Specifications Ad Hoc Task Group on High Strength Steel, December 19, American Institute of Steel Construction, Chicago, Ill.

AISC (2021), *Specification for Structural Stainless-Steel Buildings*, ANSI/AISC 370–21, American Institute of Steel Construction, Chicago, Ill.

AISC (2022a), *Code of Standard Practice for Steel Buildings and Bridges*, ANSI/AISC 303-22, American Institute of Steel Construction, Chicago, Ill.

AISC (2022b), *Specification for Structural Steel Buildings*, ANSI/AISC 360-22, American Institute of Steel Construction, Chicago, Ill.

Alpsten, G.A. (1968), "Thermal Residual Stresses in Hot-Rolled Steel Members," Fritz Engineering Laboratory Report No. 337.3, Lehigh University, Bethlehem, Pa.

ANSYS (2023), ANSYS® Mechanical APDL, Release 2023 R1, Theory Reference, ANSYS, Inc.

ArcelorMittal (2019), "High-Rise Building Brochure," ArcelorMittal Europe-Long Products, Sections and Merchant Bars, Luxembourg.

ArcelorMittal (2020), *"High-Strength Structural Shapes: ASTM A913 Grade 65 and Grade 70,"* ArcelorMittal USA. Retrieved from: https://usa.arcelormittal.com.

AS (2020), *Steel Structures*, AS 4100:2020, Standards Australia, Sydney, Australia.

ASTM (2015), *Standard Specification for Cold-Formed Welded Carbon Steel Hollow Structural Sections (HSS)*, ASTM A1085/1085M, ASTM International, West Conshohocken, Pa.

ASTM (2018a), *Standard Specification for Hot-Rolled Structural Steel, High-Strength Low-Alloy Plate with Improved Formability*, ASTM A656/656M, ASTM International, West Conshohocken, Pa.

ASTM (2018b), *Standard Specification for Structural Steel for Bridges*, ASTM A709/709M, ASTM International, West Conshohocken, Pa.

ASTM (2019a), *Standard Specification for Carbon Structural Steel*, ASTM A36/36M, ASTM International, West Conshohocken, Pa.

ASTM (2019b), *Standard Specification for High-Strength Low-Alloy Steel Shapes of Structural Quality, Produced by Quenching and Self-Tempering Process (QST)*, ASTM A913/913M, ASTM International, West Conshohocken, Pa.

ASTM (2020), *Standard Specification for Structural Steel Shapes*, ASTM A992/992M, ASTM International, West Conshohocken, Pa.

ASTM (2021a), *Standard Specification for Cold-Formed Welded and Seamless Carbon Steel Structural Tubing in Rounds and Shapes*, ASTM A500/500M, ASTM International, West Conshohocken, Pa.

ASTM (2021b), *Standard Specification for High-Strength Low-Alloy Columbium-Vanadium Structural Steel*, ASTM A572/572M, ASTM International, West Conshohocken, Pa.

Ban, H., Shi, G., Shi, Y., and Bradford, M.A. (2013), "Experimental Investigation of the Overall Buckling Behaviour of 960 Mpa High Strength Steel Columns," *Journal of Constructional Steel Research*, Vol. 88, pp. 256–266.

Bauschinger, J. (1886), "On the Change of the Elastic Limit and the Strength of Iron and Steel, by Drawing Out, by Heating and Cooling, and By Repetition of Loading (Summary)," *Minutes of Proceedings of the Institution of Civil Engineers with Other Selected and Abstracted Papers, 87*, p. 463.

Beer, H. and Schulz, G. (1975), "The European Column Curves," in *Construction Métallique*, Vol. 3.23, pp. 385–398.

Bjorhovde, R. (1972), "Deterministic and Probabilistic Approaches to the Strength of Steel Columns," PhD Thesis, Lehigh University, Bethlehem, Pa.

Boissonnade, N. and Somja, H. (2012), "Influence of Imperfections in FEM Modeling of Lateral Torsional Buckling," *Proceedings of the Annual Stability Conference*, Structural Stability Research Council, Grapevine, Texas, pp. 18–21.

CEN (2005a), *Eurocode 3: Design of Steel Structures—Part 1-1: General Rules and Rules for Buildings*, EN 1993-1-1:2005, Comite Européen de Normalisation, Brussels, Belgium.

CEN (2005b), *Eurocode 3: Design of Steel Structures—Part 1-2: General Rules—Structural Fire Design,* EN 1993-1-2:2005, Comite Européen de Normalisation, Brussels, Belgium.

Comini, D.G., Del Guidice, S., Lewis, R.W., and Zienkiewicz, O. (1974), "Finite Element Solution of Non-Linear Heat Conduction Problems with Special Reference to Phase Change," *International Journal for Numerical Methods in Engineering*, Vol. 8, No. 3, pp. 613–624.

ECCS Technical Committee 8 (2008), *The Residual Stresses in Hot-Rolled Structural Sections and Their Effect on Column Strength*, European Convention for Constructional Steelwork.

Ferreira Filho, J.O., Tankova, T., Carvalho, H., Martins, C., and da Silva, L.S. (2022), "Experimental and Numerical Flexural Buckling Resistance of High Strength Steel Columns and Beam-Columns," *Engineering Structures*, Vol. 265, pp. 114414.

Fujita, Y. (1955), "The Magnitude and Distribution of Residual Stress," Fritz Engineering Laboratory Report No. 220A.20, Lehigh University, Bethlehem, Pa.

Fukumoto, Y. and Itoh, Y. (1983), "Evaluation of Multiple Column Curves Using the Experimental Data-Base Approach," *Journal of Constructional Steel Research*, Vol. 3, No. 3, pp. 2–19.

Galambos, T.V., ed. (1998), *Guide to Stability Design Criteria for Metal Structures*, 5th Ed., Structural Stability Research Council, Wiley, New York, N.Y.

Galambos, T.V. and Ketter, R.L. (1959), "Columns under Combined Bending and Thrust," *Journal of the Engineering Mechanics Division*, Vol. 85, No. 2, pp. 1–30.

Hu, G., Morovat, M.A., Lee, J., Schell, E., and Engelhardt, M. (2009), "Elevated Temperature Properties of ASTM A992 Steel," *Proceedings of the ASCE/SEI Structures Congress 2009: Don't Mess with Structural Engineers: Expanding Our Role*, pp. 1–10.

Huber, A.W. (1956), "The Influence of Residual Stress on The Instability of Columns," Doctoral Dissertation, University Microfilms, Inc., Ann Arbor, Mich.

Huang, L., Li, G.Q., Wang, X.X., Zhang, C., Choe, L., and Engelhardt, M. (2018), "High Temperature Mechanical Properties of High Strength Structural Steels Q550, Q690 And Q890," *Fire Technology*, Vol. 54, pp. 1,609–1,628.

Jönsson, J. and Stan, T.C. (2017), "European Column Buckling Curves and Finite Element Modelling Including High Strength Steels," *Journal of Constructional Steel Research*, Vol. 128, pp. 136–151.

Khan, Q.S., Uy, B., Tao, Z., and Mashiri, F. (2013), "Concentrically Loaded Short High Strength Steel Columns with Normal and High Strength Concrete Infill," *Engineering Structures*, Vol. 49, pp. 905–917.

Lamarche, C.P. and Tremblay, R. (2011), "Seismically Induced Cyclic Buckling of Steel Columns Including Residual-Stress and Strain-Rate Effects," *Journal of Constructional Steel Research*, Vol. 67, pp. 1,401–1,410.

Li, G.Q., Wang, Y.Q., and Chen, S.W. (2012), "Experimental Study on the Overall Buckling Behavior of High Strength Steel Columns," *Journal of Constructional Steel Research*, Vol. 74, pp. 145–150.

Li, T.J., Li, G.Q., Chan, S.L., and Wang, Y.B. (2016), "Behavior of Q690 High-Strength Steel Columns: Part 1: Experimental Investigation," *Journal of Constructional Steel Research*, Vol. 123, pp. 18–30.

Ma, Y., Gardner, L., and Yuan, H. (2015), "Buckling of Ferritic Stainless Steel Members under Combined Axial Compression and Bending," *Journal of Constructional Steel Research*, Vol. 110, pp. 190–198.

Mathur, K., Fahnestock, L.A., Okazaki, T., and Parkolap, M.J. (2012), "Impact of Residual Stresses and Initial Imperfections on the Seismic Response of Steel Moment Frames," *Journal of Structural Engineering*, Vol. 138, No. 7, pp. 942–951.

Moghadam, S.J. (2015), "Plastic Buckling of Columns and Plates," Doctoral Dissertation, Department of Civil and Environmental Engineering, Imperial College London, London, U.K.

Morrison, M. (2015), "Innovative Seismic Performance Enhancement Techniques for Steel Building Moment Resisting Connections," PhD Dissertation Research, North Carolina State University, Raleigh, N.C.

Quayyum, S. and Hassan, T. (2017), "Initial Residual Stresses in Hot-Rolled Wide-Flange Shapes: A Computational Technique and Influence on Structural Performances," *Journal of Structural Engineering*, Vol. 143, No. 5, pp. 04017013.

Rasmussen, K.J.R. and Hancock, G.J. (1995), "Tests of High Strength Steel Welded I-Section Columns," *Journal of Constructional Steel Research*, Vol. 32, No. 2, pp. 167–187.

Rossi, A., Saito, D.H., Martins, C.H., and de Souza, A.S.C. (2021), "The Influence of Structural Imperfections on the LTB Strength of I-Beams," *Structures*, Vol. 29, pp. 1173–1186.

Shi, G., Ban, H., and Bijlaard, F. S. (2012), "Tests and Numerical Study of Ultra-High Strength Steel Columns with End Restraints," *Journal of Constructional Steel Research*, *70*, 236–247.

Snijder, H.H., Cajot, L.G., Popa, N., and Spoorenberg, R. C. (2014), "Buckling Curves for Heavy Wide Flange Steel Columns," *Romanian Journal of Technical Science: Applied Mechanics*, Vol. 59, No. 1/2, pp. 178–204.

Somodi, B. and Kövesdi, B. (2016), "Flexural Buckling of Cold-Formed High-Strength Steel Rectangular Hollow Section Columns," *Journal of Constructional Steel Research*, Vol. 122, pp. 614–626.

Somodi, B. and Kövesdi, B. (2017), "Flexural Buckling of Welded Box Section Columns Made of High Strength Steels," *Journal of Constructional Steel Research*, Vol. 128, pp. 567–579.

Spoorenberg, R.C., Snijder, H.H., Cajot, L.-G., and May, M.S. (2013), "Experimental Investigation on Residual Stresses in Heavy Wide Flange QST Steel Sections," *Journal of Constructional Steel Research*, Vol. 89, pp. 63–74.

Stall, K., Culhane, A., Sun, L., Cross, R.C., and Steiner, M. (2024), "Tensile Coupon Testing and Residual Stress Measurements of High-Strength Steel Built-Up I-Shaped Sections," *Engineering Journal*, AISC, Vol. 61, No. 3, pp. 159–175.

Strating, J. and Vos, H. (1975), "Computer Simulation of the ECCS Buckling Curve—Using a Monte-Carlo Method," *Construction Métallique*, Vol. 3.23, pp. 334–358.

Stroetmann, R. and Penner, G. (2024), "Buckling Resistance and Residual Stresses of Welded Box Columns Made of High-Strength Steels," *10th International Conference on Steel and Aluminum Structures (ICSAS24)*, Rio de Janeiro, Brazil.

Sun, Y., Liang, Y., and Zhao, O. (2020), "Minor-Axis Flexural Buckling Behaviour and Resistances of Pin-Ended S690 High Strength Steel Welded I-Section Columns," *Thin-Walled Structures*, Vol. 156, pp. 106980.

Tide, R.H.R. (2001), "A Technical Note: Derivation of the LRFD Column Design Equations," *Engineering Journal*, AISC, Vol. 38, No. 4, pp. 137–139.

von Kármán, T. (1907), "Festigkeitsprobleme im Maschinenbau," F. Klein and C. Müller, Eds., Vol. 4. 4, B.G. Teubner, pp. 311–385.

Wang, J. and Gardner, L. (2013), "Testing and Numerical Simulation of High Strength Steel Hollow Sections under Bending," *Journal of Constructional Steel Research*, Vol. 80, pp. 100–108.

Yun, X., Zhu, Y., Meng, X., and Gardner, L. (2023), "Welded Steel I-Section Columns: Residual Stresses, Testing, Simulation and Design," *Engineering Structures*, Vol. 282, pp. 115631.